

***Global and local parameter estimation of a model of
the electrical activity of the heart***

Valérie Moreau-Villéger — Hervé Delingette — Maxime Sermesant — Owen Faris —
Elliot McVeigh — Nicholas Ayache

No 5269

20 juillet 2004

Thème BIO



***apport
de recherche***



Global and local parameter estimation of a model of the electrical activity of the heart

Valérie Moreau-Villéger^{*}, Hervé Delingette^{*}, Maxime Sermesant^{†*}, Owen Faris[‡], Elliot McVeigh[‡], Nicholas Ayache^{*}

Thème BIO — Systèmes biologiques
Projet EPIDAURE

Rapport de recherche no 5269 — 20 juillet 2004 — 51 pages

Abstract: In this article we study the problem of estimating the parameters of an electrical model of the heart from a temporal recording of extracellular potentials. The chosen model is the reaction-diffusion model on the action potential proposed by Aliev and Panfilov. The strategy consists in building an error criterion based upon a comparison of depolarization fronts between the model and the measures. This error criterion is minimized by a global and then local adjustment of the model parameters. The feasibility of the approach is demonstrated on simulated and real measures on a canine heart.

Key-words: heart modeling, electrophysiology, inverse problem, data assimilation, parameter estimation, FitzHugh-Nagumo, electrical conductivity

^{*} EPIDAURE research project, INRIA Sophia Antipolis, France

[†] Computation Imaging Science Group, King's College, London, England

[‡] Laboratory of Cardiac Energetics, National Heart Lung and Blood Institute, National Institute of Health, Bethesda, Maryland, USA

Estimation de paramètres globaux et locaux pour un modèle de l'activité électrique du cœur

Résumé : Dans cet article, nous nous intéressons au problème de l'estimation des paramètres d'un modèle électrique du cœur à partir d'un enregistrement temporel de potentiels extracellulaires. Le modèle choisi est le modèle de réaction-diffusion du potentiel d'action proposé par Aliev et Panfilov. La stratégie employée s'appuie sur le choix d'un critère d'erreur. Ce critère est basé sur la comparaison entre les fronts de dépolarisation issus du modèle et des mesures. Ce critère est ensuite minimisé par un ajustement global puis local des paramètres du modèle. La faisabilité de cette approche est démontrée sur des données synthétiques et des données réelles d'un cœur de chien.

Mots-clés : électrophysiologie, modélisation cardiaque, assimilation de données, estimation de paramètres, FitzHugh-Nagumo, electrical conductivity, inverse problem

Contents

1	Introduction	4
1.1	Comparing models and measures in electrophysiology	4
1.2	Estimation of electrical conductivity as an inverse problem	5
2	Modeling and simulating the electrical activity of the heart	6
2.1	Modeling at the macroscopic level	6
2.2	Numerical implementation issues	7
2.3	Theoretical influence of the parameters on the depolarization times	9
3	Global estimation of the parameter k	10
3.1	Method	10
3.2	Results on simulated data	13
4	Local estimation of the electrical conductivity	13
4.1	Context	13
4.2	Method	16
4.3	Regional estimation	18
4.4	Computation of the matrix $\mathbf{M}^k = [\partial \mathbf{t} / \partial d_R]$	19
4.5	Simulated data	21
4.6	Example 1: Estimation of the conductivity value for small perturbations of the initial conductivity value	25
4.7	Example 2: Estimation of a conductivity value far from the initial conductivity value	25
4.8	Example 3: Estimation of one conductivity value for a non homogeneous region	29
4.9	Summary	30
5	Results on real measures	30
5.1	Surgery and Experimental Layout	30
5.2	Data Acquisition	31
5.3	Depolarization times computation	32
5.4	Adjusting the initial conditions	32
5.5	Global estimation of k parameter	33
5.6	Local estimation of the conductivity	34
5.7	Relevance of the computed conductivity	34
5.8	Accuracy of the depolarization times	41
6	Conclusions and perspectives	41
	Appendix A Numerical implementation of the finite elements methods	46

1 Introduction

Direct models of the electrical activity of the heart are numerous ([Nob02, BM04, AP96, SNH01, CFGPT98, KFB+03, BWZ+02, KPE04, TNNP03]). Since direct *in vivo* measures are becoming available ([MFE+01, MSTM01]), the next challenge is to solve the inverse problem. The aim is to find the parameters of a model that best fit the measures obtained from a specific patient. Not only coupling real measures with a model allows for a real validation of the model, but also estimating the parameters for a specific patient provides a help for diagnosis and localization of electrical pathology as well as for intervention planning.

1.1 Comparing models and measures in electrophysiology

In electrophysiology, there are usually three different types of electrical potential that can be considered : the extracellular potential, the intracellular potential and the transmembrane potential or action potential. The cardiac cells are separated of their environment by a membrane. This membrane separates two electrical environments. The intracellular and the extracellular domains have different ionic concentrations and therefore different potentials, the intracellular and the extracellular potentials. This difference creates a transmembrane potential or action potential. The action potential is the electrical potential leading to the contraction of cardiac fibers and can be considered as the "main command" of the mechanical function of the heart. For this reason, the measurement and computation of the action potential is crucial to assess the cardiac function.

The use of electrodes positioned on the endocardium, epicardium or pericardium (as shown in ([MFE+01, MSTM01])) leads to the measurement of the extracellular potential but not directly the action potential. However, electrophysiological models that include the computation of both intracellular and extracellular potentials, called bidomain models [SNH01], are considered as being complex mathematically and numerically. For this reason (see section 2 for more details), we chose a simpler model, the Aliev-Panfilov model [AP96], that describes the action potential propagation during the cardiac cycle.

To validate the action potential computation based on the Aliev-Panfilov model, we compare the depolarization and the repolarization times extracted from electrophysiological measures and those extracted from the computational model. The depolarization time is the time when a cardiac cell becomes activated, leading to fiber contraction. The repolarization time is the time when a cardiac cell returns to its rest potential, leading to fiber relaxation. The depolarization times can be computed from the extracellular potential measures, as explained in [SFE+03], by taking the instant where the time derivative is the most negative (Figure 1). From action potential, the depolarization time of a point is the first instant when the action potential is over a threshold (cf. Figure 1). Note that some models [KFB+03], directly compute the depolarization times.

The repolarization time is not always easy to detect from the measured extracellular potential. Therefore we only address, in this report, the comparison of the depolarization times.

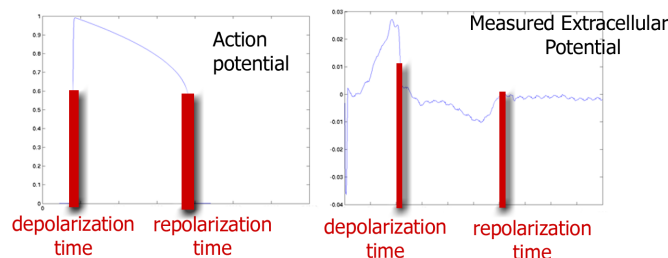


Figure 1: Comparing simulated action potential (left) and measured extracellular potential (right) on one electrode.

1.2 Estimation of electrical conductivity as an inverse problem

When inspecting electrophysiology data, cardiologists often base their analysis on the depolarization and repolarization maps of the epicardium or endocardium and more specifically on isochrones associated with both instants [Rud01]. From those maps, expert eyes can detect different electrophysiological pathologies ranging from the presence of low conduction zones caused by infarcted tissue, to the occurrence of fibrillation caused by scrolling waves.

The aim of the research effort presented in this paper is to provide cardiologists with additional information for a better diagnosis and a better planning of therapies. This additional information can be a dense conductivity map of the endocardium leading to the early detection of damaged cardiac tissue, or a precise location of ectopic focus or reentry points leading to an optimal planning of radio-frequency ablation.

To achieve this task we do not resort to using a pure signal processing approach, where for instance conduction could be estimated from the distance of two isochrone curves. Indeed, such straightforward approaches, though helpful, do not provide significant added value from the original data. Instead, we propose to compute this additional information by solving an inverse problem : finding the parameters (including local electrical conductivity) of a cardiac electrophysiology model that can best explain electrophysiological observations (isochrones).

By inverting such a model, we can expect two important outcomes. First, we aim at estimating "hidden" physical parameters (conductivity for instance) from an original set of physical parameters (time of depolarization). Second, with this set of parameters, we can use the direct model for preventing pathologies and for planning therapy.

We report in this paper preliminary results concerning the inversion of the Aliev-Panfilov electrophysiological model leading to the regional estimation of conductivities. We first describe this model and detail its numerical implementation (Section 2). Then we achieve a coarse estimation (Section 3) of the k parameter that properly scales the electrical propagation. Then we perform the regional estimation of the conductivity in Section 4 by minimizing an error function between the measured and simulated depolarization times. A case study on a dog heart in Section 5 shows the efficiency of the proposed approach for

inverting the Aliev-Panfilov electrophysiological model. Finally, we summarize and present the perspectives of this work in Section (6).

2 Modeling and simulating the electrical activity of the heart

2.1 Modeling at the macroscopic level

In normal conditions, the myocardial cells are electrically coupled allowing the propagation of the action potential in the ventricle. At the cell level, the main objective is to study the relationship between the transmembrane ionic currents and the ionic potentials inside and outside the cell. The models concerning this relation become more and more complete as the number of phenomena observed at the cell level increases [ABC96].

In its basic formulation, a cellular model is only expected to account for the most important biological phenomena:

- a cell is activated only for a stimulus larger than a certain threshold;
- the shape of the action potential does not depend on the stimulus (it is only model-dependent);
- there is a refractory period during which the cell cannot be excited;
- a cell can act as a pacemaker.

Different kinds of model are available in the literature ([NR01, BM04, Nob02, KPE04]). Between the simple two variables FitzHugh-Nagumo model [Fit61] to the models of Luo-Rudy [LR91, LR94] which include many ionic currents to precisely represent the evolution of the potentials lies for example the Beeler-Reuter model [BR77], the first biophysical model taking into account the specific ionic channels of the ventricular cells with eight variables. There are also computationally efficient models like [FK98, BWZ⁺02] that do not retain all the details of each ionic current and that are more accurate than the FitzHugh-Nagumo model. In bidomain models [Tun78, SNH01], extra-cellular *and* intra-cellular potentials are included. These models have many more parameters than simple mono-domain models like the FitzHugh-Nagumo model.

To adjust parameters of the model from macroscopic measures, a global model is sufficient. Actually, the subtle phenomena modeled in accurate cellular models like Luo and Rudy models [LR91, LR94] are not available from macroscopic measures. Moreover, with a complex model, we would have too many parameters to estimate given the number of measures available. A FitzHugh-Nagumo like model [Fit61] fits the previous expectations and allows to perform reasonably fast 3D computations of the action potential propagation. Aliev and Panfilov developed a modified version of the FitzHugh-Nagumo equations suited

to the cardiac action potential and to the changes in pacing frequency [AP96]:

$$\begin{aligned}\varepsilon^2 \partial_t u &= \varepsilon \operatorname{div}(D \nabla(u)) + ku(1-u)(u-a) - uz & (1.a) \\ \partial_t z &= -(ku(u-a-1) + z) & (1.b)\end{aligned}\tag{1}$$

where u is a normalized action potential and z is a dynamic variable modeling the repolarization, k controls the repolarization, ε controls the coupling between the action potential and the repolarization variable z and a controls the reaction phenomenon. Typical values of those parameters can be found in [AP96].

With an excitation above the initialization threshold, an action potential is initiated and propagates in the epicardium surface. The anisotropy of the ventricles can be taken into account through the diffusion tensor D : $D = d_0 \operatorname{diag}(1, \rho, \rho)$ in a local orthonormal basis (\mathbf{i} , \mathbf{j} , \mathbf{k}) where \mathbf{i} is parallel to the fiber direction, d_0 is a scalar conductivity and ρ the anisotropy ratio between the transverse and the axial conductivities.

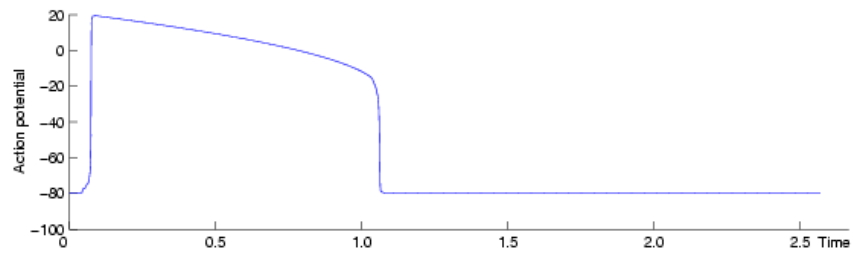
The simulated action potential with this system (Figure 2(a)) is similar to the one observed in animal and human measurements of cardiac action potentials as on Figure 2(b). These measures were performed on a frog cardiac cell [RP82]. This 3D anisotropic model was developed in the context of the ICEMA collaborative research action (ICEMA/ICEMA-2 <http://www-rocq.inria.fr/sosso/icema2/icema2.html>) [ACC⁺01, SFP⁺02, SCD⁺01, CCG⁺01]. A qualitative validation of this model of the electrical front propagation was performed in [SFE⁺03] which consists of a comparison with Durrer measures and *in vivo* measures.

2.2 Numerical implementation issues

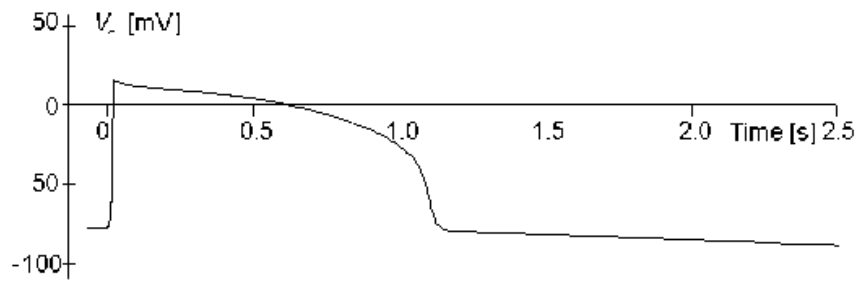
Since the electrophysiological measures are available on the endocardium or the epicardium, we propose to simulate the Aliev and Panfilov model on a surface. In the remainder, we consider a surface triangulation \mathcal{S} with N vertices and L triangles. We call \mathcal{V} the set of vertices and \mathcal{T} the set of the triangles. However we model a propagation on the 2D surface of the epicardium whereas the propagation of the depolarization wave is a tridimensional propagation. Taking into account the fibers directions in this very coarse model would not improve significantly the accuracy of the model. For this reason, we use an isotropic propagation: $D = d_0 \operatorname{diag}(1, 1, 1)$ in Equation (1).

The variables x and t of the system of Aliev and Panfilov as presented in (1) are normalized so that x and t vary between 0 and 1. For a simulation on a real anatomical surface, the system is scaled spatially to the maximum dimension of the mesh and temporally so that the action potential duration is around 0.3 s ($\tau = 0.26t$, with τ the real time and t the normalized time). Since the system of Aliev and Panfilov (Equation (1)) is dimensionless, the parameters are also dimensionless, in particular the electrical conductivity d_0 . The other parameters are: $\varepsilon = 0.1$, $a = 0.15$. The choice $\varepsilon = 0.1$ guarantees a stable scheme even for the very coarse mesh provided by the measures. We will adjust k globally in Section 3 and the electrical conductivity d locally in Section 4.

In a normal heart, the ventricles are first excited through the Purkinje Network. In this article we are in the frame of artificial pacing. In both cases, we need to isolate the surface



(a)



(b)

Figure 2: Comparison between the shape of a simulated action potential (a) and an action potential measured on a frog cardiac cell [RP82] (b).

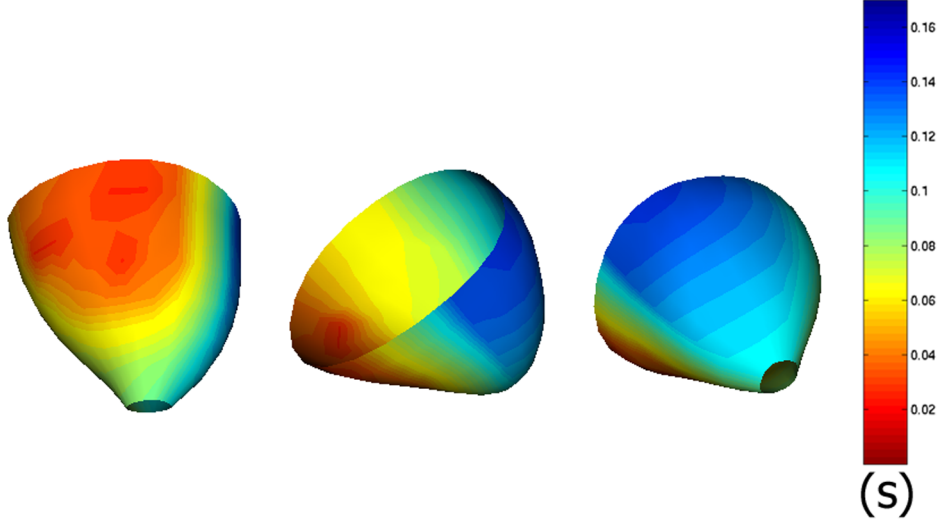


Figure 3: A surface mesh where the depolarization time is computed for each vertex after simulating the action potential propagation. The color encodes the depolarization times.

region where the propagation begins in order to set the initial conditions. Once this region is selected, the initialization consists in putting a positive potential in this region during a small time interval.

The spatial integration is performed with the finite elements method. We use linear triangular elements with 3 vertices. The discretization is detailed in Appendix A. The temporal integration of the system (1) is done with an explicit Euler scheme. With the notations of Appendix A, we get:

$$\begin{cases} u^{t+\Delta t} &= u^t + \frac{\Delta t}{\varepsilon} [-l^2 \varepsilon^2 \mathcal{M}^{-1} \mathcal{K} u^t (1 - u^t)(u^t - a) - u^t z^t] \\ z^{t+\Delta t} &= z^t + \Delta t [-k u^t (u^t - a - 1) + z^t] \end{cases} \quad (2)$$

From the output of the simulations, we compute the depolarization times by thresholding the action potential. These depolarization times are not sensitive to the choice of the threshold since the depolarization is a very fast phenomenon.

Figure 3 presents an example of simulated depolarization times on an epicardial surface.

2.3 Theoretical influence of the parameters on the depolarization times

Since our final objective is the estimation of the parameters of the Aliev-Panfilov system (1) from the measured depolarization times (Figure 3), we are interested in the influence of

the different parameters of Equation (1) on the depolarization times. Reaction diffusion systems and especially the FitzHugh-Nagumo system of equations have already been widely mathematically studied. For example [Kee86, Mur02] provide surveys of the properties of this system.

Equation (1.a) is the depolarization equation. In the absence of any repolarization ($z = 0$), the Aliev-Panfilov model is the same as the classical FitzHugh-Nagumo model:

$$\varepsilon \partial_t u = \varepsilon^2 \partial_x (d \partial_x u) + ku(1 - u)(u - a) \quad (3)$$

Equation (3) is called the Nagumo equation and its solutions are wave fronts traveling at a velocity c given by

$$c = \sqrt{2kd}(0.5 - a) \quad (4)$$

However the repolarization equation perturbs this simple situation. We checked on 1D simulations that Equation (4) was still a good approximation for the velocity of the depolarization wave for the complete model and our surface geometry. Thus we made several simulations with different values of parameters a , k , d and ε and for each set of parameters we have computed the velocity of the depolarization wave. We noticed that ε did not influence the velocity, as predicted in Equation (4). We also found that the influence of the repolarization equation on the velocity was not significant. Figure 4 shows the comparison between the estimated and the theoretical velocities as a function of two parameters a and k . In Figure 4(a), the velocity is not always well-defined because numerical instabilities occur for some choice of those parameters (time step and grid size are kept constant whereas the stability condition depends on the parameters). Consequently, for some parameters, no solution is obtained and the velocity is not defined as in the dark blue areas of Figure 4(a). When both velocities are available, we visually check that there is a good agreement between the simulated velocity and the theoretical velocity for a large range of parameters a and k .

3 Global estimation of the parameter k

The parameter ε is chosen according to the grid size but the parameters of the model a , k , or d can vary between individuals or species. Hence it is not possible to use a standard set of parameters for all clinical case. Therefore we first have to adjust these parameters in order to scale the propagation in the time and space.

3.1 Method

At this stage we use the theoretical arguments on the Aliev and Panfilov system introduced in Section 2: Equation (4) gives the velocity of the depolarization wave $c(d, k, a)$ on a 1D domain. In 2D, James Keener proved in [Kee86] that the velocity of the depolarization wave is not homogeneous in space. At one specific point, it is equal to the velocity in 1D

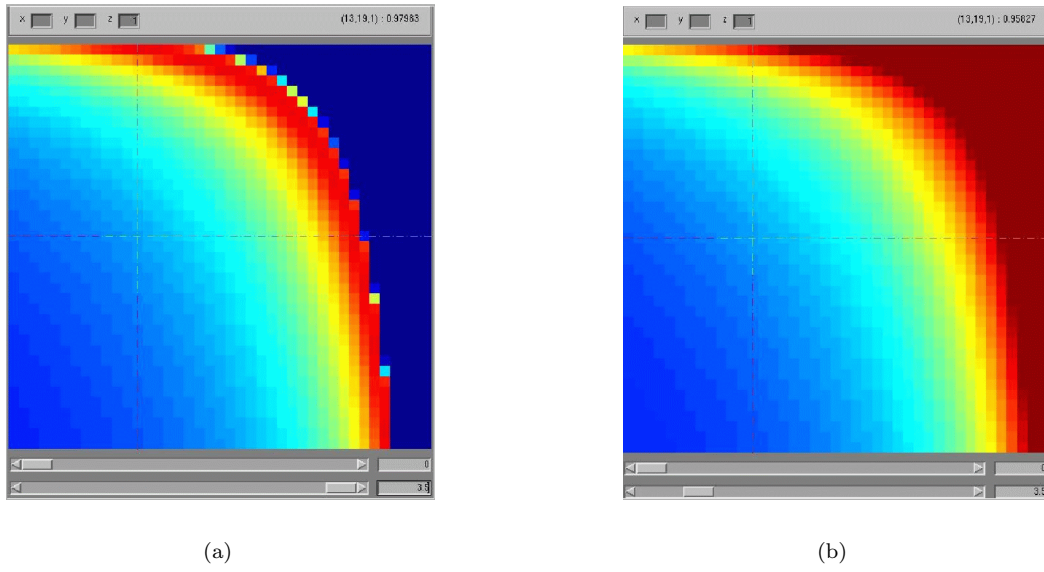


Figure 4: Comparison between the propagation velocity estimated from 1D simulations of the Aliev-Panfilov system (a) and the theoretical propagation velocity computed with Equation (4) (b). The color encodes the velocity of the propagation wave. X-axis: parameter a . Y-axis: parameter k .

(Equation 4) minus a correction proportional to the curvature of the front. The Aliev-Panfilov model is very close to the FitzHugh-Nagumo model concerning the depolarization wave and we also observe in our simulations that the velocity is dependent on the curvature of the front, especially near the pacing vertices where the curvature of the front is high. But we just need a global estimate of the propagation velocity in a surface. Therefore, as a first approximation, we neglect the front curvature at this stage and simply consider that Equation 4 is globally valid, i.e. $c = \sqrt{2kd}(0.5 - a)$.

Fortunately, the depolarization velocity can also be computed from the measured depolarization times. Equation (5) holds

$$\frac{1}{c} = \|\nabla_{\mathbf{x}} t\|. \quad (5)$$

and we can compute the gradient $\nabla_{\mathbf{x}} t$ in the surface mesh according to Appendix A. With the same notations, on each triangle $tr = (\mathbf{P}_0 \mathbf{P}_1 \mathbf{P}_2)$, the gradient of t is

$$\nabla_{\mathbf{x}} t(tr) = \sum_{i=0}^2 \nabla \varphi_i t(\mathbf{P}_i).$$

We denote $\mathcal{SH}(v)$ the shell of the vertex v , that is the set of triangles to which v belongs. Then for each vertex $v \in \mathcal{V}$, the gradient $\nabla_{\mathbf{x}} t$ is given by

$$\nabla_{\mathbf{x}} t(v) = \frac{\sum_{tr \in \mathcal{SH}(v)} \nabla_{\mathbf{x}} t(tr) \mathcal{A}(tr)}{\sum_{tr \in \mathcal{SH}(v)} \mathcal{A}(tr)}$$

where $\mathcal{A}(tr)$ is the area of triangle tr .

We use Equation (5) to estimate a median value of the k parameter. From equations (4) and (5), we get:

$$\text{median}(\|\nabla_{\mathbf{x}} t\|)^{-1} = \sqrt{2kd}(0.5 - a). \quad (6)$$

Having only one equation, we first choose to estimate globally only parameter k . The other parameters are fixed.

A direct inversion of Equation (6) would be a comparison between a theoretical 1D value and an estimated value on a 2D surface. We rather use a velocity estimated from a first guess simulation computed with the same mesh as the measures. From Equation (4), we can see that the velocity c is proportional to $1/\sqrt{k}$. Consequently, Equation (6) induces that $\text{median}(\|\nabla_{\mathbf{x}} t\|)^{-1}$ is proportional to \sqrt{k} . We then have

$$\frac{\text{median} \|\nabla_{\mathbf{x}} t^m\|}{\text{median} \|\nabla_{\mathbf{x}} t^s\|} = \frac{c^s}{c^m} \approx \frac{\sqrt{k^s}}{\sqrt{k^m}}.$$

with t^m the measured depolarization times, t^s the simulated depolarization times, k^s the parameter used for the first guess simulation, c^s the median propagation velocity for the first guess simulation, c^m the median propagation velocity computed from the measures and

k^m the parameter k underlying the measured depolarization times. Then k^m is computed with the following equation.

$$k^m = k^s \left(\frac{\text{median } \|\nabla_{\mathbf{x}} t^s\|}{\text{median } \|\nabla_{\mathbf{x}} t^m\|} \right)^2 \quad (7)$$

3.2 Results on simulated data

We evaluate the performance of the above algorithm on simulated data. We use as electrophysiological measures the depolarization times computed from a simulated propagation.

The depolarization times presented on Figure 3 were computed from the Aliev and Panfilov model with $k = 12$. To be more realistic, we used a non homogeneous conductivity map with values around 1.0. For all parameters but k , we choose standard parameters that can be found in the literature like in [AP96].

Figure 5 presents the gradient computed from the simulated measures as explained before. Applying the previously described procedure to this simulated data, we obtain a global value of $k^m = 12.51$ starting from a crude initialization $k^s = 8$. a and ε for the crude initialization were chosen equal to the parameters used to compute Figure 3, and the conductivity d was chosen homogeneously equal to 1.0. The resulting value is close to the expected value since we used a correct value for a and an approximate value for d . Since the velocity $c = \sqrt{2kd}(0.5 - a)$, a , k and d are not observable independently observable. Then the accuracy of the above algorithm is not evaluated from the accuracy on k but from the average absolute error between the depolarization times. From 25.3 ms with $k^s = 8$ it drops to 14.7 ms with the new estimated value $k^m = 12.51$.

As we can see on Figure 6, the regions where the error on the depolarization times are very large get smaller after the global estimation of k . After the estimation of k , the error on the depolarization times displayed in Figure 6(b) is small near the pacing region. But on the other side of the epicardium, at the end of the propagation, the error is still very large. The reason is that a small difference in the velocity induces a long term difference for the depolarization times.

4 Local estimation of the electrical conductivity

4.1 Context

Since we only have one reliable measure per vertex (the depolarization time), we can locally estimate at most one parameter to fit given measurements of depolarization times. We choose the electrical conductivity d as the spatially varying parameter. Despite the fact that the electrical conductivity d is a relative value, the local variations of the conductivity have a physiological meaning. Regions where the conductivity is abnormally small are of clinical interest. We see the problem of the local estimation of the conductivity from patient specific data as part of the field of data assimilation. Data assimilation consists of combining dynamical models with real observations to improve the knowledge of the system under study.

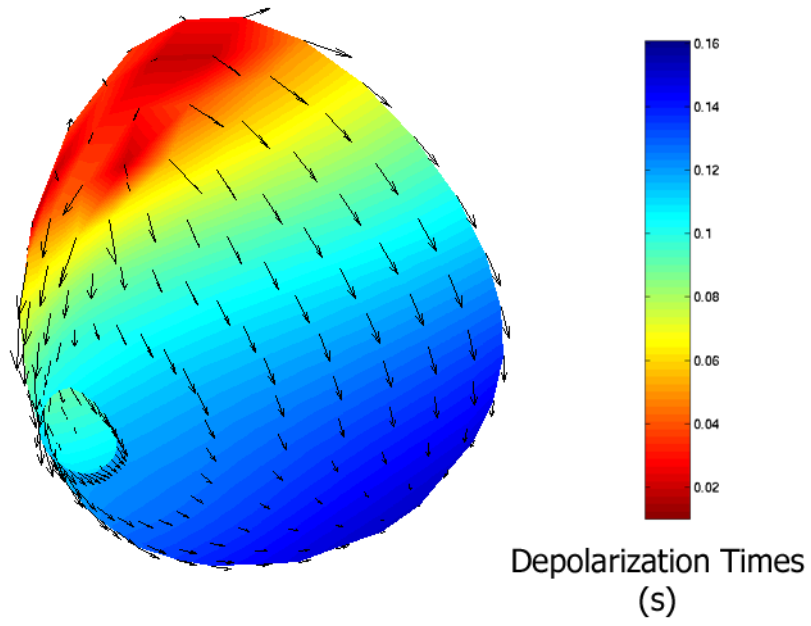
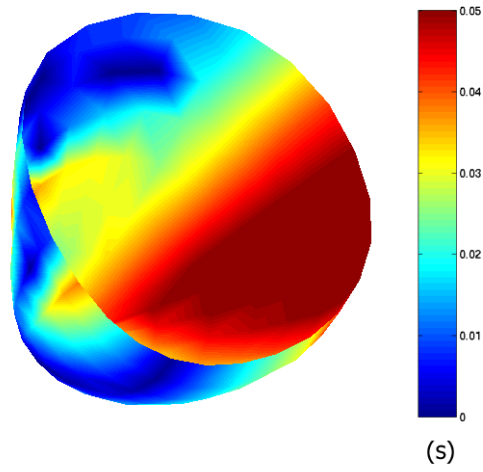
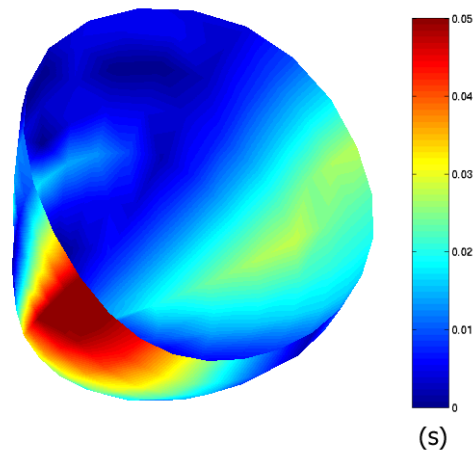


Figure 5: Gradient of a depolarization time map computed at each vertex. The color represents the depolarization times and the arrows represent $\nabla_{\mathbf{x}}t$.



(a)



(b)

Figure 6: Absolute error on the depolarization times between measures and simulations before(a) and after (b) the global automatic estimation.

Data assimilation was successfully applied in different fields such as meteorology, oceanography, financial mathematics, motion estimation. Recently, data assimilation methods were introduced in the biomechanical study of the heart as in [SL02] for the mechanical part. Data assimilation is based on the minimization of the error between the measures and the model. There are two main classes of methods:

1. variational methods based on the theory of optimal control [Lio68]. These methods consist in performing a global minimization over the entire time interval.
2. sequential methods consist in correcting the system each time a measure is available. These methods are organized around Kalman filtering ([Kal60, May79]) Suboptimal filters were derived since, like Extended Kalman Filter, SEEK or particular filters [PVR97, BBH⁺03, BEW03, vdMW01].

None of the classical methods of data assimilation are really suited for the model and the measures of our problem. The criterion C that we want to minimize here is the difference between the depolarization times extracted from the *measures* (called t^m) and the one extracted from the *simulated* action potential (called t^s).

$$C = \sum_{v \in \mathcal{V}} |t_v^m - t_v^s|^2.$$

Since the time variable has a specific signification in Kalman filtering, it cannot be applied directly to our problem where the measures are depolarization **times**. Similarly, variational methods that deal with the whole cardiac cycle are not suitable either because the propagation of the depolarization wave is causal. So we keep one of the idea of Kalman Filtering by estimating the parameters region by region, following the propagation of the depolarization wave. Then on each region, we minimize the difference between the depolarization times.

4.2 Method

Conductivity values are assigned to each triangle of the surface. Consequently, we look for a conductivity value for each triangle. We pose the problem as finding the conductivity map $\mathbf{d} = (d_j)_{0 \leq j \leq L-1}$ that minimizes $C(\mathbf{d})$:

$$C(\mathbf{d}) = \sum_{v \in \mathcal{V}} |t_v^m - t_v(d_0, \dots, d_{L-1})|^2 \quad (8)$$

where t_v^m is the measured depolarization time at vertex v and $t_v(d_0, \dots, d_{L-1})$ the depolarization time at vertex v resulting from a simulation with the conductivities (d_0, \dots, d_{L-1}) .

We start from a simulation obtained with an initial homogeneous conductivity \mathbf{d}^0 , with $d_j^0 = 1.0$ for all $0 \leq j \leq L-1$, and the global parameters k , a and ε that were set as explained in the previous section. A simulation with this set of parameters provides an initial depolarization times map: $\mathbf{t}^0 = (t_v^0)_{v \in \mathcal{V}}$. When we slightly perturb the conductivity

on all triangles, the following approximation holds, for all vertices v :

$$t_v(d_0^0 + \delta d_0, \dots, d_{L-1}^0 + \delta d_{L-1}) = t_v^0(d_0^0, \dots, d_{L-1}^0) + \sum_{j=0}^{L-1} \frac{\partial t_v}{\partial d_j}(d_0^0, \dots, d_{L-1}^0) \delta d_j \quad (9)$$

Equation (9) can be expressed in matricial form:

$$\mathbf{t} = \mathbf{t}^0 + \mathbf{M}^0 \delta \mathbf{d} \quad (10)$$

where

$$\mathbf{M}^0 = \left[\frac{\partial \mathbf{t}}{\partial \mathbf{d}}(\mathbf{d}^0) \right] = \left[\frac{\partial t_v}{\partial d_j}(d_0^0, \dots, d_{L-1}^0) \right]_{v \in \mathcal{V}, 0 \leq j \leq L-1},$$

$\mathbf{t} = (t_v(d_0^0 + \delta d_0, d_1^0 + \delta d_1, \dots, d_{L-1}^0 + \delta d_{L-1}))_{v \in \mathcal{V}}^T$, and $\delta \mathbf{d} = (\delta d_j)_{0 \leq j \leq L-1}^T$. If we write the difference between the initial depolarization times and the measured depolarization times $\delta \mathbf{t}^0 = (t_i^m - t_i^0)_{v \in \mathcal{V}}$, then we search a conductivity map $\mathbf{d}^1 = \mathbf{d}^0 + \delta \mathbf{d}$ that minimizes $\mathcal{E}(\delta \mathbf{d})$:

$$\mathcal{E}(\delta \mathbf{d}) = \sum_{v \in \mathcal{V}} |t_v^m - t_v^0 - \sum_{j=0}^{L-1} \frac{\partial t_v}{\partial d_j} \delta d_j|^2 = \|\mathbf{t}^m - \mathbf{t}^0 - \mathbf{M}^0 \delta \mathbf{d}\|^2 \quad (11)$$

The solution of this mean square minimization problem is given by

$$\delta \mathbf{d} = ((\mathbf{M}^0)^T (\mathbf{M}^0))^{-1} (\mathbf{M}^0)^T \delta \mathbf{t}^0 \quad (12)$$

We then obtain a first approximation of the conductivity with:

$$\mathbf{d}^1 = \mathbf{d}^0 + ((\mathbf{M}^0)^T (\mathbf{M}^0))^{-1} (\mathbf{M}^0)^T \delta \mathbf{t}^0 \quad (13)$$

Since the linearization that is applied in Equation 9 is only valid for small perturbations of \mathbf{d} , we propose an iterative process which alternates a linearization (Equation (10)) and then a minimization (Equation (12)). Let \mathbf{d}^k be the conductivity map at iteration k , \mathbf{t}^k the depolarization times vector at iteration k . At each iteration k , the criterion $\mathcal{E}^k(\delta \mathbf{d})$:

$$\mathcal{E}^k(\delta \mathbf{d}) = \sum_{v \in \mathcal{V}} |t_v^m - t_v^k - \sum_{j=0}^{L-1} \frac{\partial t_v}{\partial d_j} \delta d_j|^2 = \|\mathbf{t}^m - \mathbf{t}^k - \mathbf{M}^k \delta \mathbf{d}\|^2 \quad (14)$$

```

Data : the number of iterations  $it$ , an initial guess  $\mathbf{d}^0 = 1.0$ 
Result: the new conductivity  $\mathbf{d}^{it}$ 
Initialization  $\mathbf{d}^0 = 1.0$  everywhere ;
for  $k = 0 \rightarrow it$  do
    Compute the depolarization times  $\mathbf{t}^k$  with the conductivity map  $\mathbf{d}^k$ ;
    Estimation of  $\mathbf{M}^k$ ;
    Compute  $\delta \mathbf{d} = ((\mathbf{M}^k)^T (\mathbf{M}^k))^{-1} (\mathbf{M}^k)^T \delta \mathbf{t}^k$ ;
    Update the conductivity  $\mathbf{d}^{k+1} = \mathbf{d}^k + \delta \mathbf{d}$ 
end

```

Algorithm 1: Iterative estimation of the conductivity.

4.3 Regional estimation

If we estimate one conductivity value for each triangle, we would have more degrees of freedom than electrical measures. Therefore we split the heart surface into different connected regions and estimate one conductivity value d_R on each region R : $d_j = d_R$ for all j such that the j^{th} triangle tr_j belongs to the region R .

Moreover the propagation of the depolarization wave on the heart is a causal problem. Instead of estimating simultaneously the conductivities of the different regions, we estimate the conductivity one region after another. Thus, when we estimate a conductivity value on a region R , all the regions that were previously depolarized are already processed. During the estimation of the conductivity value d_R on region R , the conductivity values of the other regions remain constant.

Then for one region R , the criterion of Equation (14) to be minimized at iteration k becomes:

$$\mathcal{E}(\delta d_R) = \sum_{v \in \mathcal{V}} |t_v^m - t_v^k - \frac{\partial t_v}{\partial d_R} \delta d_R|^2. \quad (15)$$

In this case the matrix \mathbf{M}^k is a vector : $\mathbf{M}^k = [\partial t_v / \partial d_R]_{v \in \mathcal{V}}^T$. Then criterion of Equation (15) can be written:

$$\mathcal{E}^k(\delta d_R) = \|\mathbf{t}^m - \mathbf{t}^k - \mathbf{M}^k \delta d_R\|^2. \quad (16)$$

As a consequence d_R^{k+1} is given by:

$$d_R^{k+1} = d_R^k + ((\mathbf{M}^k)^T (\mathbf{M}^k))^{-1} (\mathbf{M}^k)^T \delta \mathbf{t}^k \quad (17)$$

For a regional estimation, we propose the following iterative algorithm: Algorithm 2

```

Data : the number of iterations  $it$ , the partition of the surface in regions  $\mathcal{R}$ , an
         initial guess  $\mathbf{d}^0 = 1.0$ 
Result: A new conductivity map  $d_R^{it}$  for all the regions
for  $R \in \mathcal{R}$  do
    Initialization  $d_R^0 = 1.0$  ;
    for  $k = 0 \rightarrow it$  do
        Compute the current depolarization time map  $\mathbf{t}^k$ . Estimation of  $\mathbf{M}^k$ ;
        Compute  $\delta d_R^k = ((\mathbf{M}^k)^T (\mathbf{M}^k))^{-1} (\mathbf{M}^k)^T \delta \mathbf{t}^k$ ;
        Update the conductivity  $d_R^{k+1} = d_R^k + \delta d_R^k$  ;
    end
end

```

Algorithm 2: Regional conductivity estimation algorithm.

4.4 Computation of the matrix $\mathbf{M}^k = [\partial \mathbf{t} / \partial d_R]$

There is still an unknown in Algorithm 2, we did not detail the computation of a value or an approximation for $\mathbf{M}^k = [\partial t_v / \partial d_R]_{v \in \mathcal{V}}$ at the current state, for the region R . There is no simple analytical relationship between conductivity and depolarization times that can be derived because the depolarization times are obtained by thresholding the solution of the PDEs of Equation (1). We thus need a numerical estimation of $[\partial \mathbf{t} / \partial d_R]$ based on centered finite differences. For each vertex $v \in \mathcal{V}$:

$$\frac{\partial t_v}{\partial d_R} \approx \frac{t_v(d_R + \Delta d) - t_v(d_R - \Delta d)}{2\Delta d} \quad (18)$$

To compute $\mathbf{t}(d_R + \Delta d)$ and $\mathbf{t}(d_R - \Delta d)$, we modify the conductivity on the given region R respectively to $d_R + \Delta d$ and $d_R - \Delta d$, and perform two new simulations. In theory, the smaller Δd is chosen, the more accurate is this estimation. But if Δd is too small, $\mathbf{t}(d + \Delta d) \approx \mathbf{t}(d - \Delta d)$ and the estimated derivative could be 0. Consequently, for the computation of the derivative by finite differences with Equation (18) to be stable, Δd cannot be chosen arbitrarily small.

Figure 7 gives an example of the derivative of the depolarization times according to the conductivity on a small region. This example presents some more general properties.

- First we observe that $\partial t_v / \partial d_R$, is nearly zero in a large area. The contribution of this area in the criterion of Equation (19) is almost null, \mathbf{M}^k is therefore a sparse matrix. As a consequence, we do not need to use all the depolarization times of the mesh to estimate a reliable value for the conductivity.
- We can see that the area where the derivative is significantly different from 0 (*influence area of the conductivity modification*) lies mainly behind the region of interest. This is due to the fact that we model a causal phenomenon, the propagation of the

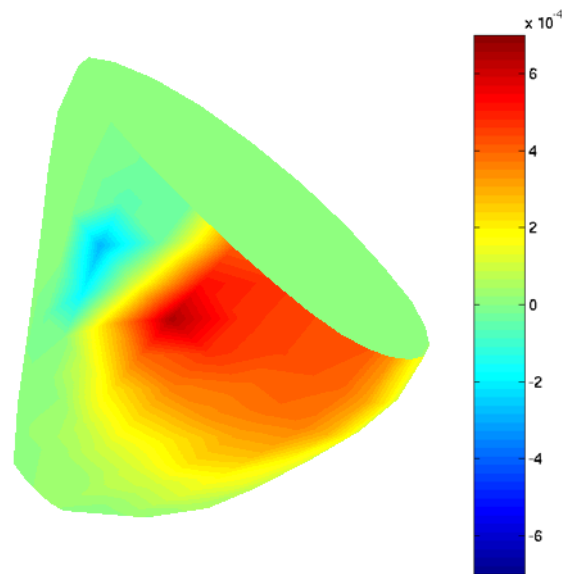


Figure 7: Derivative of depolarization times according to the conductivity on a small region. The derivative is computed with finite differences. From negative values (blue) to positive values (red) with a large region where the derivative is zero (green).

depolarization wave in the heart. So the modification of a conductivity value on a region implies modifications of the depolarization times only in the regions behind the region of interest.

- We observe that the derivative is negative. Indeed, the propagation velocity increases with the conductivity. Consequently, the depolarization times have to decrease with the conductivity.
- Just before the region where the conductivity was modified, we notice a small region where the derivative is positive but small. This can be explained by use of a reaction-diffusion models which compute the action potential and do not include the causality of the propagation of the depolarization wave. Therefore, modifications of the conductivity on a region R create a modification of the depolarization times even before the region R , but of limited extent.

As a consequence, we only use the vertices of the region of interest R and some of their neighbors to estimate a conductivity value. This set of vertices is denoted $E(R)$ (Figure 8). Furthermore, by restricting the set of vertices where the depolarization time is computed, we can significantly speed-up the whole conductivity estimation, since we can stop the simulation as soon as the farther vertices have been depolarized. Then, instead of minimizing the criterion $\mathcal{E}^k(\delta d_R)$ of Equation (14), we minimize:

$$\mathcal{E}^k(\delta d_R) = \sum_{v \in E(R)} |\mathbf{t}_v^m - \mathbf{t}_v^k - \frac{\partial t_v}{\partial d_R} \delta d_R^k|^2 \quad (19)$$

Therefore $\delta \mathbf{t}^k$ becomes $\delta \mathbf{t}^k = (t_v^m - t_v^k)_{v \in E(R)}^T$, $\mathbf{M}^k = (\partial t_v / \partial d)_{v \in E(R)}^T$ in Algorithm 2.

Figure 9(a) presents an example of the depolarization times as a function of the conductivity d_R at the seven vertices of a region R and Figure 9(b) presents the derivative $\partial t / \partial d$ of these curves. It is obvious from Figure 9(a) that this function is nonlinear. $\partial t / \partial d$ has a strong influence on the expected accuracy for the conductivity estimation. These values are quite small, which means that large modifications of the conductivity d are necessary to obtain significant differences on the depolarization times. As a consequence, we have here an intrinsic limitation on the maximum accuracy we can hope to obtain on the conductivity d . We also notice that the derivative is greater for small values of d than for large values of d . Consequently, we can estimate more accurately small conductivity values than larger ones.

4.5 Simulated data

We apply the algorithm 2 in the case of simulated data. We choose a small region R (Figure 10) where the conductivity value is modified from the standard value to a value d_R^m . We then want to estimate a conductivity value for this region using only the simulated depolarization times. We work on simulations computed with standard parameters :

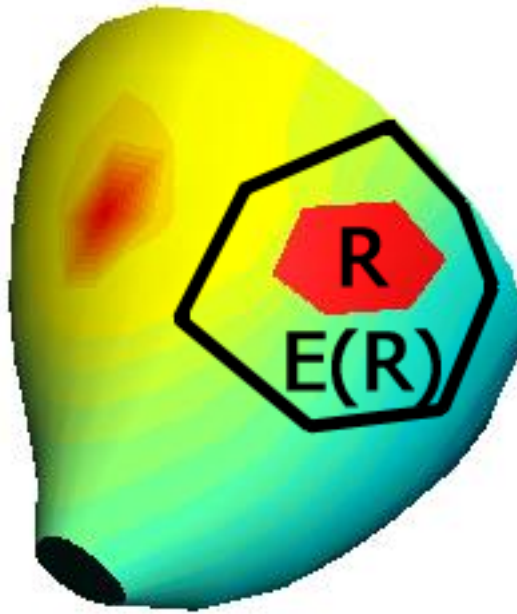
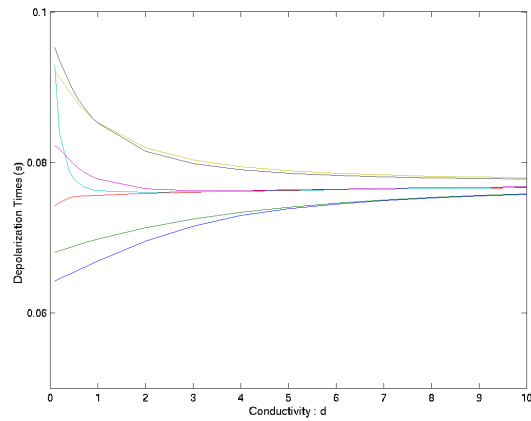
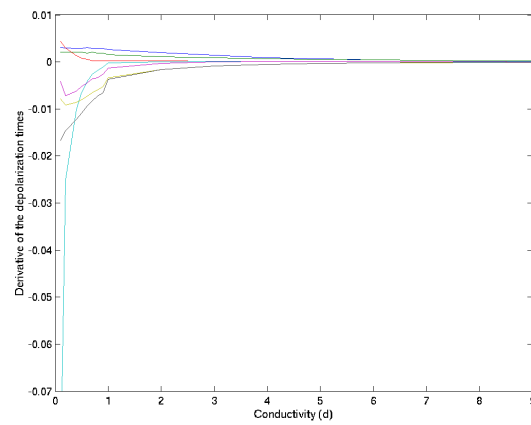


Figure 8: The current region of interest R and the set of neighboring vertices $E(R)$ that we choose to perform the estimation of d_R .



(a)



(b)

Figure 9: Evolution of the depolarization times for each vertex of the region of interest for different conductivity values. On the left (a) Depolarization times versus conductivity. On the right (b) Derivative of the depolarization times versus conductivity.

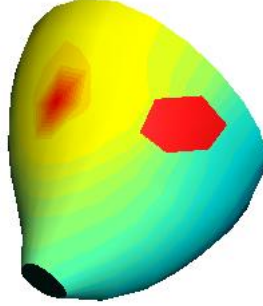


Figure 10: Surface region where the conductivity has been modified.

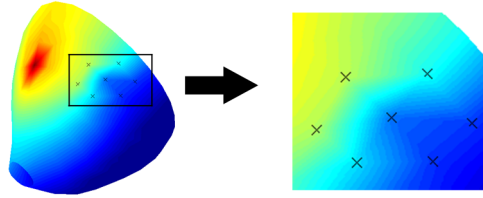


Figure 11: Example of simulated measures. The crosses represent the electrodes (i.e. the vertices) where the depolarization times are extracted $E(R)$. On the right, a close-up on region R .

a	0.15
ε	0.1
k	15
d	1

We perform a new simulation with a modified conductivity value, then threshold the action potential and finally produce a map of depolarization times \mathbf{t}^m (left of Figure 11) that we consider as input to the conductivity estimation algorithm. In this example, we suppose that we know where the conductivity has been modified, the region R . We need to choose the set $E(R)$ of vertices where the depolarization times are used. We choose $E(R)$ to be the vertices of the region R (right of Figure 11). We then perform estimations of the conductivity for different values of d_R^m and of the discretization step Δd for the computation of $\partial t / \partial d_R$ according to Algorithm 2.

4.6 Example 1: Estimation of the conductivity value for small perturbations of the initial conductivity value

In this first example, we estimate the conductivity on R for four different conductivity values, $d_R^m \in \{0.5, 0.75, 0.9, 2.0\}$ and for different values of Δd . Figure 12 displays the evolution of the conductivity during algorithm 2 for four values of d_R^m : 0.9, 0.75 and 0.5. and 2.0.

Only a few iterations are necessary for the estimated conductivity to be close to the expected value, whatever Δd . Furthermore, after a few iterations, the estimated conductivity value does not change anymore. At that stage, the difference between measured and simulated depolarization times is so small that the conductivity is not modified by Equation (12). Consequently different values for Δd lead to different conductivity values as with $d_R^m = 0.9$ (cf. Figure 12(a)). In this case, the different values for Δd provide estimations of the conductivity d between 0.90 and 0.91 and we cannot expect a better accuracy on the conductivity d . Nevertheless, when the process is over, the error on d is under 2% for the worst Δd and the maximum error on the depolarization times is less than 10^{-12} s. We assess numerically the limitation of accuracy of the conductivity that we predicted in section 4.4.

From Figure 12, we also notice that a small Δd does not guarantee a better accuracy on the estimation of d_R and with a smaller Δd , the convergence is reached with more iterations. This apparent waste of computation time is counterbalanced by a better stability. Indeed, it implies smaller modifications of the conductivity at each iteration of the algorithm. Consequently, the approximation performed in Equation (9) around the current conductivity value is valid during the entire algorithm. This does not affect the previous examples because the ground truth d_R^m was already only a small perturbation from $d_R^0 = 1.0$.

4.7 Example 2: Estimation of a conductivity value far from the initial conductivity value

We now present two examples where the ratio d_R^0/d_R^m differs greatly from 1. The first example is with $d_R^m = 0.1$. This example is physiologically interesting since we aim at detecting regions with conductivity defects, for example with an infarct. There is also a technical interest. One of the conditions for the Aliev-Panfilov system to produce an action potential is that $d > 0$. If $d = 0.0$, the depolarization wave does not penetrate inside the region and if $d < 0.0$, the solution of the PDEs (1) is not an action potential. As a consequence, for numerical reasons, if d is too small, some triangles are never depolarized and we cannot estimate a conductivity value. Thus, for this example we have to keep the conductivity positive during the algorithm. Since the behavior of the depolarization times is very different for large conductivity values, we introduce a second example where $d_R^m = 5.0$.

Whereas we could choose any conductivity step for the previous examples, the choice of Δd is very important here. The expected value is far from the initial value. When Δd is too large, the estimated δd_R is often overestimated with unpleasant consequences. The estimated conductivity oscillates around the expected value with a large amplitude. The conductivity value leaves the range of parameters that produces an action potential. The

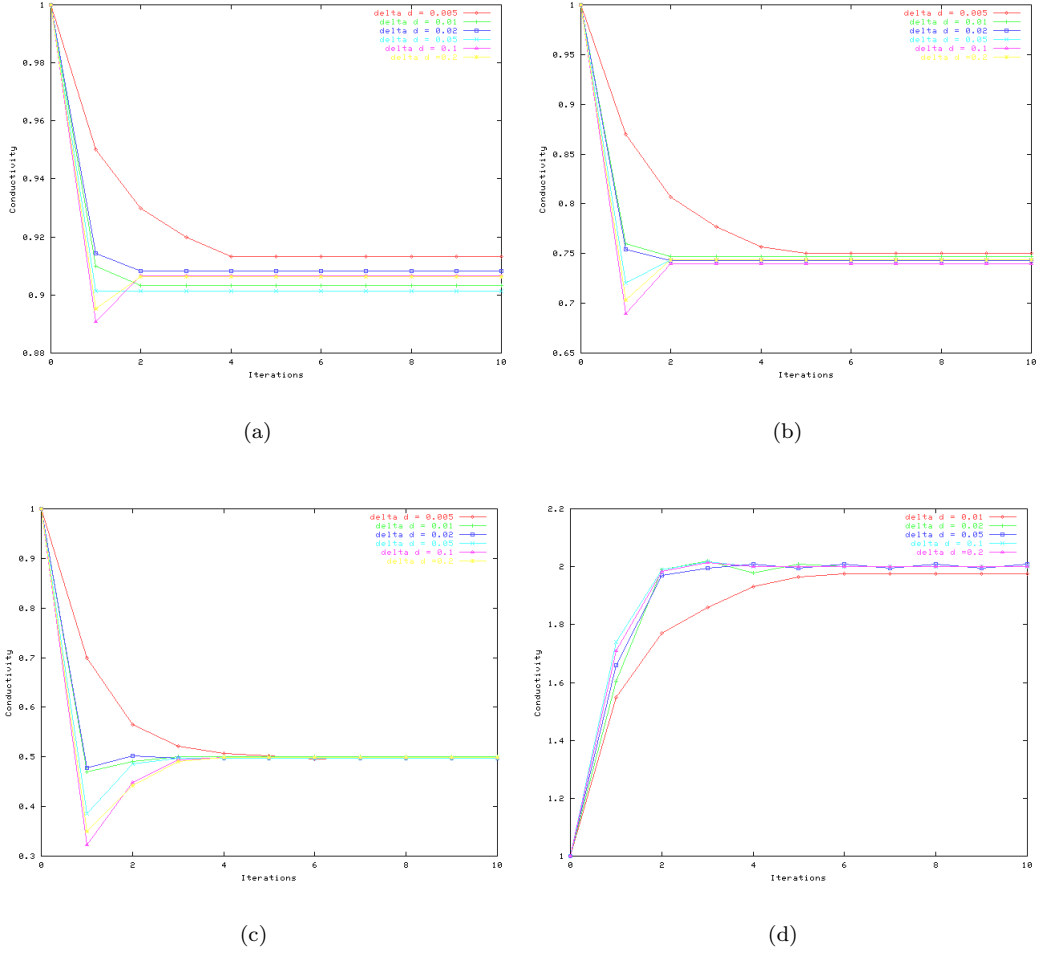
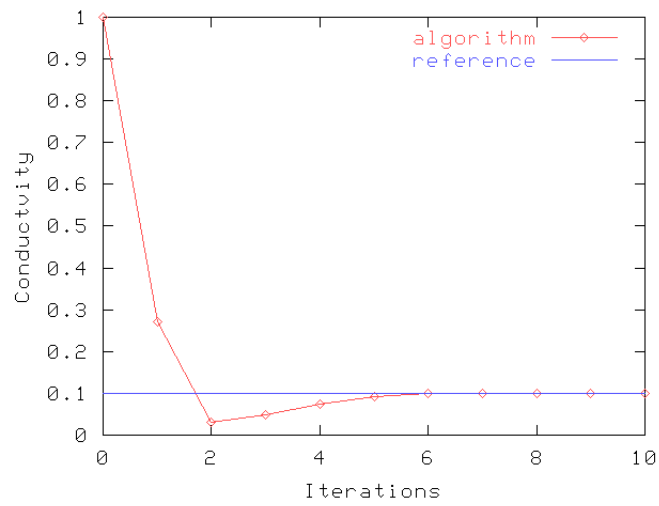
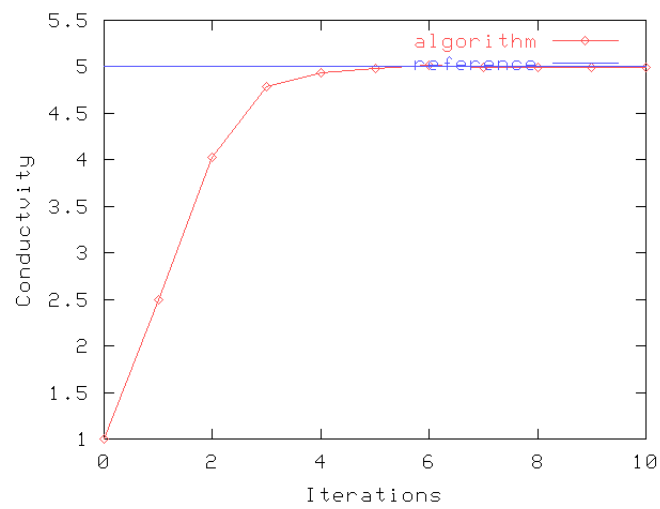


Figure 12: Estimation of the conductivity for different conductivity values d_R^m . For each experiment, the figure displays the conductivity versus the iterations for different values of Δd from 0.005 to 0.2. (a) Expected conductivity value: $d_R^m = 0.9$. (b) Expected conductivity value: $d_R^m = 0.75$. (c) Expected conductivity value: $d_R^m = 0.5$. (d) Expected conductivity value: $d_R^m = 2.0$.



(a)



(b)

Figure 13: Convergence of the conductivity estimation algorithm for $d_R^m = 0.1$ (a) and $d_R^m = 5.0$ (b).

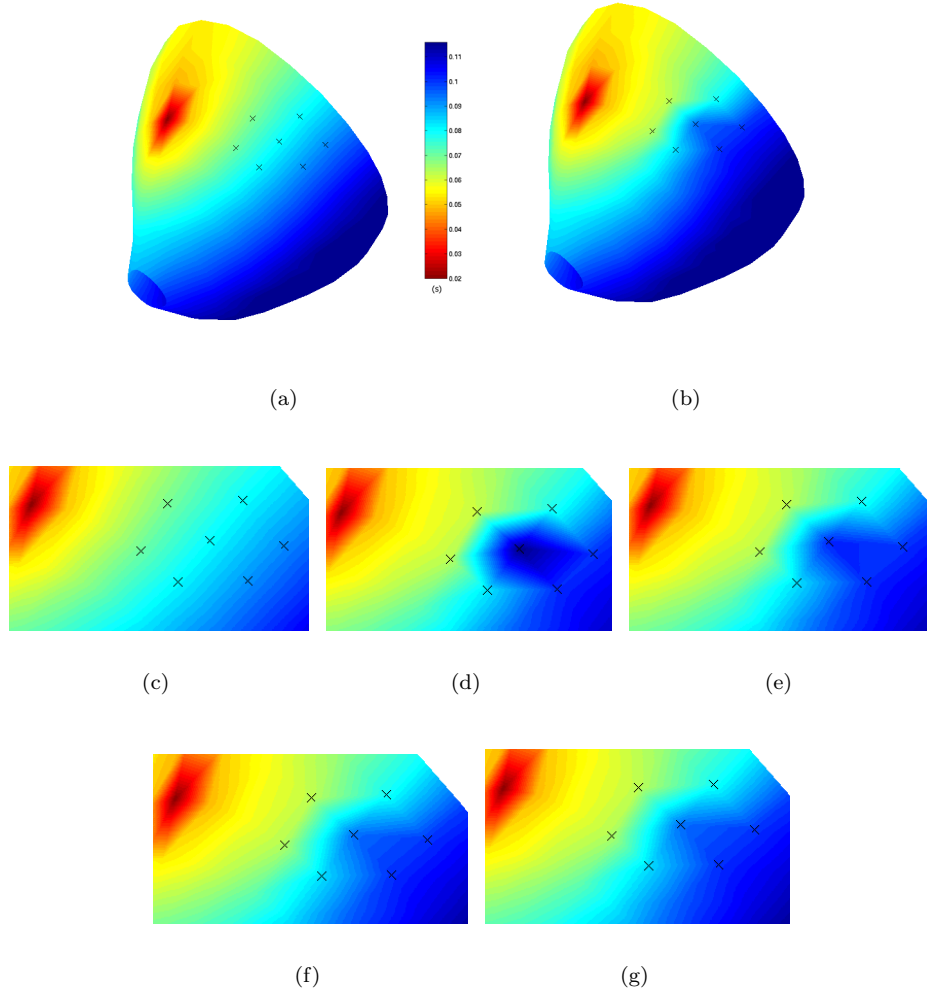


Figure 14: Depolarization times obtained during the estimation process. $d_R^m = 0.1$. (a) Initialization, $d = 1.0$ everywhere. (b) Simulated measures. (c) Initialization (close up) (d) Second iteration, $d = 0.03$ on the region of interest. (e) Fourth iteration, $d = 0.07$ on the region of interest. (f) Seventh iteration, $d = 0.1001$ on the region of interest. (g) Simulated measures.

stability conditions are not fulfilled and the propagation of the action potential fails. To preserve stability, we choose a small value for Δd .

Figure 13 presents the evolution of the estimated conductivity value during the algorithm for these two examples. Figure 14 presents a few intermediate depolarization times obtained during the conductivity estimation process for $d_R^m = 0.1$.

The conductivity estimation algorithm converges slowly as we can see on Figure 13, but the conductivity values are estimated accurately in both cases. On the example $d_R^m = 0.1$ (Figure 13(a)), we notice that d_R is underestimated at the first iteration despite the small Δd , but the next iterations lead to a correct conductivity value. The choice for Δd is different in these two cases. Since $\partial t / \partial d$ is higher for small d , we can choose a very small Δd for the example with $d_R^m = 0.1$ (Figure 13(a)). But for large values of d_R^m , like for the example $d = 5.0$, $\partial t / \partial d$ is smaller. Δd must be larger (Figure 13(b)) for the approximation of the derivative $\partial t / \partial d$ to stay different from 0.

As far as the depolarization times are concerned, within a few iterations, the difference between the measured and simulated depolarization times are visually unperceivable even with a close up on the region as shown in Figure 14. The maximum error on the depolarization times is already less than 10^{-5} s.

4.8 Example 3: Estimation of one conductivity value for a non homogeneous region

The previous examples are very simple compared with real measures. The simulated measures are obtained by assigning the same electrical conductivity value to an entire region, whereas for real measures, the “real” underlying electrical conductivity is not identical on the region where we estimate it. We want to check that we can reliably estimate one conductivity value on a region where the conductivity is nearly but not exactly constant.

Therefore, we compute artificial measures by simulating the model with different conductivities values for the different triangles of the region R pictured in Figure 10. We chose six values for the six different triangles of R between 0.5 and 0.63, with a mean value of 0.55. We then apply the algorithm described in Algorithm 2 to estimate one single conductivity value on the entire region. We can see the results on Figure 15. Just a few iterations are necessary to obtain a conductivity value near the expected value $d_R \approx 0.55$. Small oscillations around this value still remains after 4-5 iterations but the amplitude of these oscillations remains less than 10^{-4} . Thus we expect our method to cope with non homogeneous conductivity, like in real data.

4.9 Summary

We presented a method (cf. Algorithm 2) to estimate the electrical conductivity region by region. This method proved to estimate very accurately the conductivity value for one region from simulated depolarization times. The method coped with conductivity value larger or smaller than the initial value. We also showed that the algorithm still converges for measures synthesized with non homogeneous conductivity.

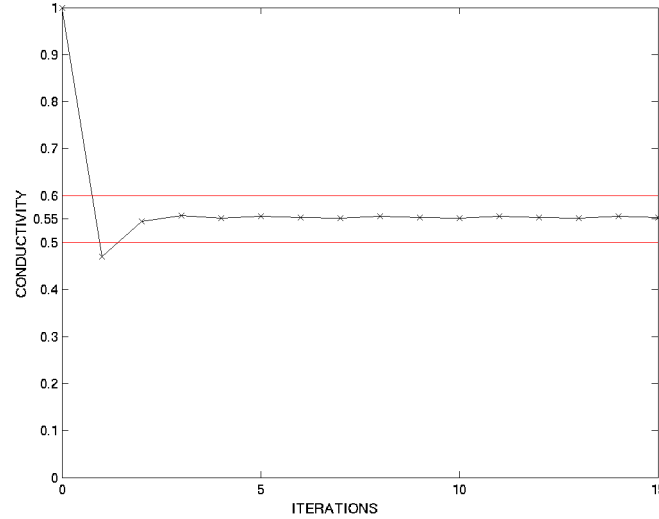


Figure 15: Convergence of the conductivity. Case of non homogeneous conductivity on the region. Expected estimated conductivity: $d \approx 0.55$.

We presented the influence of the parameter Δd on the accuracy of the estimation. Whereas the influence of Δd on the precision is not relevant, it is clear that for the sake of stability, Δd must be as small as possible provided that $\mathbf{t}(d - \Delta d)$ and $\mathbf{t}(d + \Delta d)$ are still distinguishable.

The computation of this estimation lies almost exclusively in performing simulations. For each iteration we need

- two simulations for the computation of the derivative.
- one simulation with the current conductivity to perform the comparison with measures.

The matrix operations that we perform concern small dimensions matrices, and the only matrix inversion that we need is in fact a scalar inversion. We need about 2 minutes to perform the estimation of one conductivity value for one region on a dual processor 1 GHz Pentium PC.

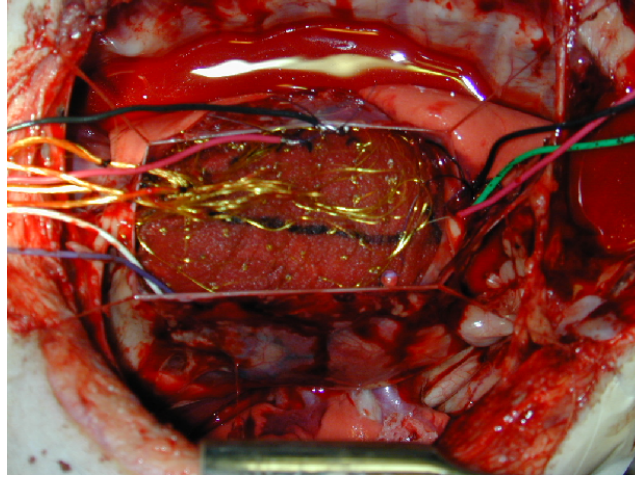


Figure 16: Multi-electrode epicardial sock on the canine heart studied, *in vivo*.

5 Results on real measures

5.1 Surgery and Experimental Layout

An adult male mongrel dog was used in this measure study. Anesthesia was induced with an initial intravenous injection of thiopental (25 mg/ml at 0.5ml/kg) and maintained after endotracheal intubation with isoflurane (0.8-2%, Siemens ventilator, 900D). A median sternotomy was performed, and a pericardial cradle was fashioned.

A multi-electrode epicardial sock consisting of a nylon mesh and 128 copper electrodes attached in an ordered fashion was then placed over the ventricular epicardium. The sock was placed in a consistent and pre-determined orientation and secured with several sutures (see Figure 16). Bipolar epicardial twisted-pair pacing electrodes were sewn onto the right atrium (RA). Similar electrodes were sewn onto the RV free-wall. A ground reference electrode was sewn onto the fat pad at the root of the aorta.

All sock and pacing wires were run directly out of the chest and connected, via a customized connection box, to two 64-channel analog to digital converter (A/D) boards (Hewlett-Packard, now Agilent, E1413C). All A/D boards were connected via FireWire (IEEE 1394) to a computer (Windows NT, 4.0) running data acquisition software (Hewlett-Packard, VEE 5.0). This procedure is MR compatible and fully detailed in [OEE+03].

5.2 Data Acquisition

RV pacing capture was established at a pacing rate (110-125 bpm) approximately 10-20% above intrinsic rate. Pacing current was set to approximately 20% above that needed for

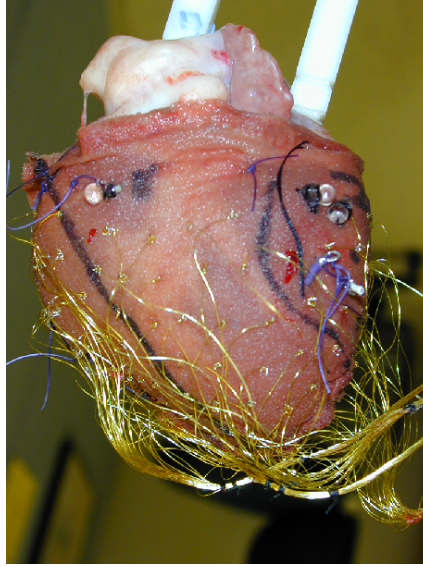


Figure 17: Sock on the canine heart studied, once excised and polysiloxane-filled.

capture. Intrinsic electrical activation was suppressed by simultaneously pacing the RA and unipolar epicardial electrical recordings were obtained.

Electrical recordings were obtained at an acquisition rate of 1000-1450 Hz for a duration of approximately 10 seconds immediately prior to and following MR scans. Unipolar signals were electrically referenced to the aortic ground electrode.

After all *in vivo* image data and electrical recordings were obtained, the animal was heparinized and then euthanized with a bolus of potassium chloride while still under general anesthesia. The heart was excised with the sock still in place. The coronary arteries were then perfused from the aorta with isotonic saline at 50-60 mmHg to induce tissue turgor, and the heart was submerged in an isotonic saline bath to reduce body force deformation.

With the excised heart therefore in an approximate end-diastolic configuration, the LV and RV were then filled with vinyl polysiloxane by injection through the corresponding atria and atrioventricular valves to fix the shape. After approximately ten minutes, the vinyl polysiloxane solidified (see Figure 17). Using a 3D digitizer, the sock electrodes and localization markers were localized (digitizer coordinates). Additionally, locations of anatomical landmarks such as inter-ventricular sulcus, apex and aortic root were recorded.

5.3 Depolarization times computation

For analysis of electrical activation, epicardial readings from each electrode were averaged over approximately 20 heartbeats. The five-point finite difference estimate of the derivative

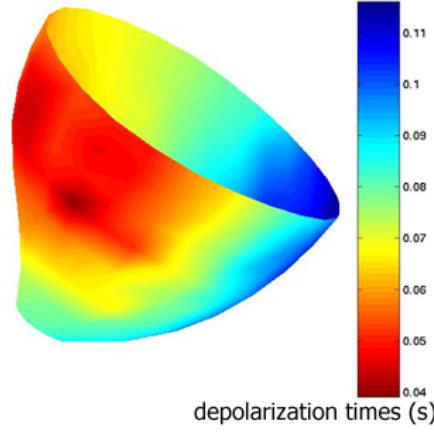


Figure 18: Interpolated depolarization times.

of the recorded voltage, v , as a function of time, t , was used:

$$\frac{dv(t)}{dt} = \frac{1}{12\Delta t}[-v(t + 2\Delta t) + 8v(t + \Delta t) - 8v(t - \Delta t) + v(t - 2\Delta t)]$$

Electrical activation times, referenced to the pacing stimulus, were chosen as the point of the most negative derivative, indicating the time of local depolarization. Due to pacing artifact, the first ten milliseconds after pacing were not used for the detection of activation times.

The depolarization times computed from the potentials recorded on the 128 electrodes of the sock are interpolated on a 336 triangles surface mesh as in Figure 18.

5.4 Adjusting the initial conditions

The first step toward a local estimation of the parameters is a good initialization. The initialization of the Aliev-Panfilov equations is performed by sending an electrical potential $u(t)$ to the vertices of the pacing regions during a small time interval. The propagation does not depend on the shape of the initial potential $u(t)$. But it is very sensitive to the localization of the pacing regions. Our goal is to find parameters that explain the propagation shape. If the error on the initial condition is too large, the parameters that we estimate will mainly come from the compensation of this error rather than from the shape of the propagation front. For that purpose, we select from the measures (Figure 18) the points with the smallest depolarization times. In the case of the measures of Figure 18, we choose three excitation regions as shown on Figure 19. There is a delay between the beginning of the recording and the excitation. We use the same delay in our simulation. We recover that delay by taking the smallest depolarization time.

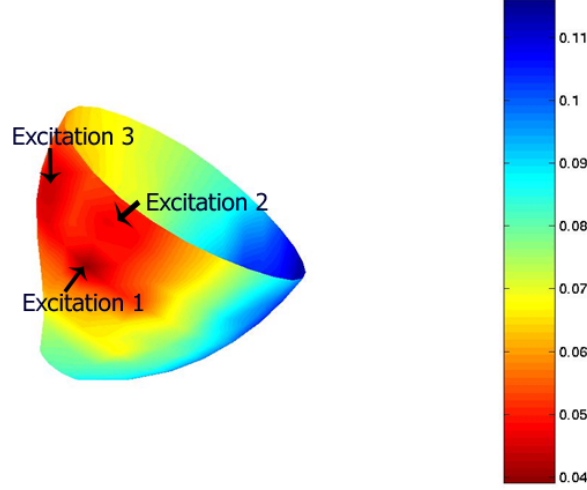


Figure 19: Excitation regions chosen to initialize the simulations. The color encodes the depolarization time in s.

5.5 Global estimation of k parameter

We compute the gradient of the depolarization times (Figure 20). Applying the method presented in Section 3.1 to the data, we obtain a global value of $k^m = 25.2$ starting from a crude initialization $k^s = 8$.

Figure 21 presents the depolarization times obtained before and after the automatic global estimation procedure. Visually, we can already see that the depolarization times obtained with our automatic procedure are in the right range of values. This is confirmed by computing the absolute error between depolarization times obtained with a simulation and depolarization times obtained from the measures. Figure 22 presents the error on the depolarization times obtained before and after the automatic global estimation procedure. Before the estimation (Figure 22(a)), the mean error is 20.6 ms. After the automatic estimation (Figure 22(b)), the mean error is 10 ms compared to the total duration of the depolarization wave duration which is around 120 ms.

The electrical propagation occurs in the good time and space scale, as we can visually check on Figure 21. But there are still large errors on some particular regions visible in Figure 22(b)..

5.6 Local estimation of the conductivity

We now apply the method described in Algorithm 2 to perform the local estimation of the conductivity. On that purpose, we need to partition the epicardium in different regions.

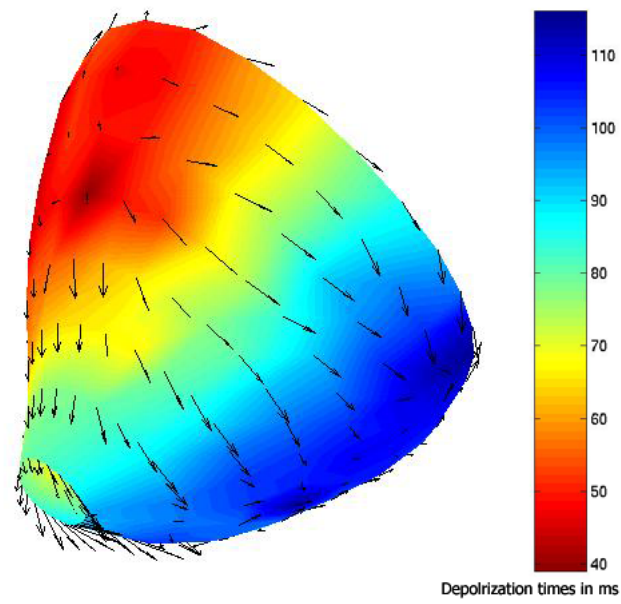
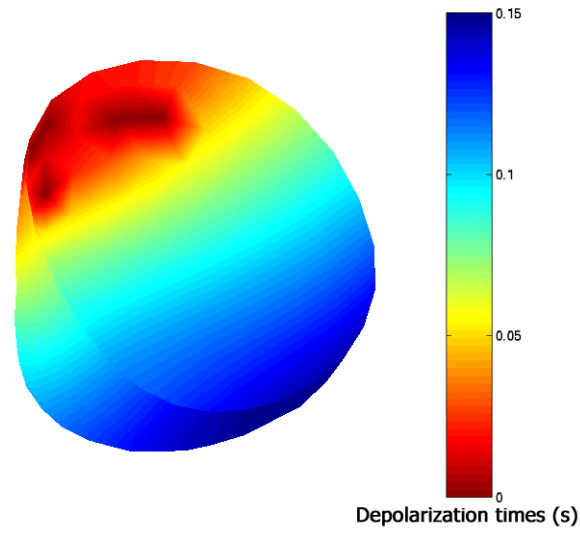
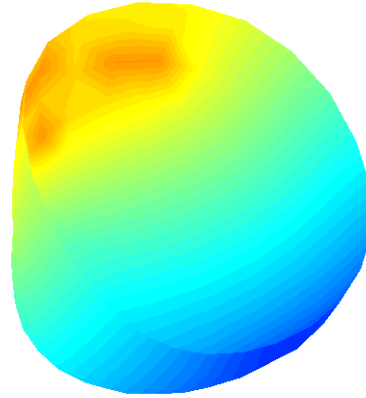


Figure 20: Gradient of a depolarization time map computed at each vertex. The color represents the depolarization times and the arrows represent $\nabla_{\mathbf{x}} t$.

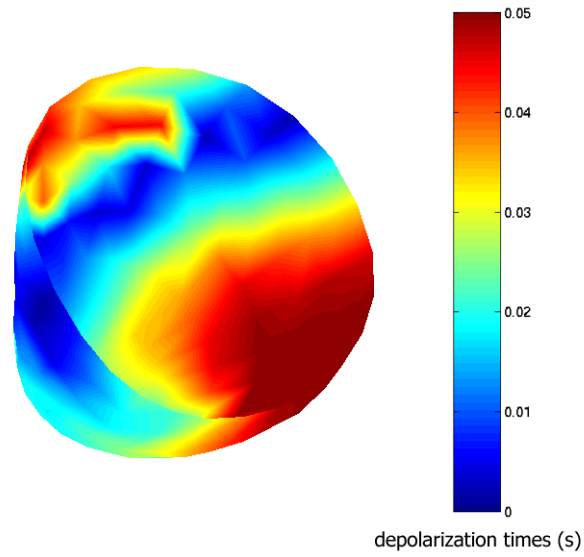


(a)

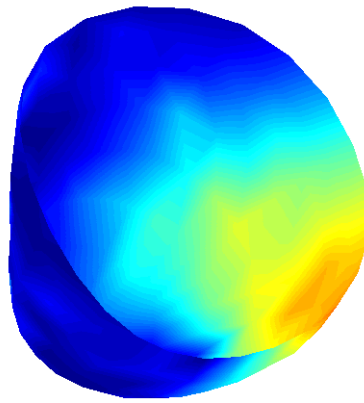


(b)

Figure 21: Depolarization times before (a) and after (b) the global automatic estimation.



(a)



(b)

Figure 22: Absolute error on the depolarization times between measures and simulations before (a) and after (b) the global automatic estimation.

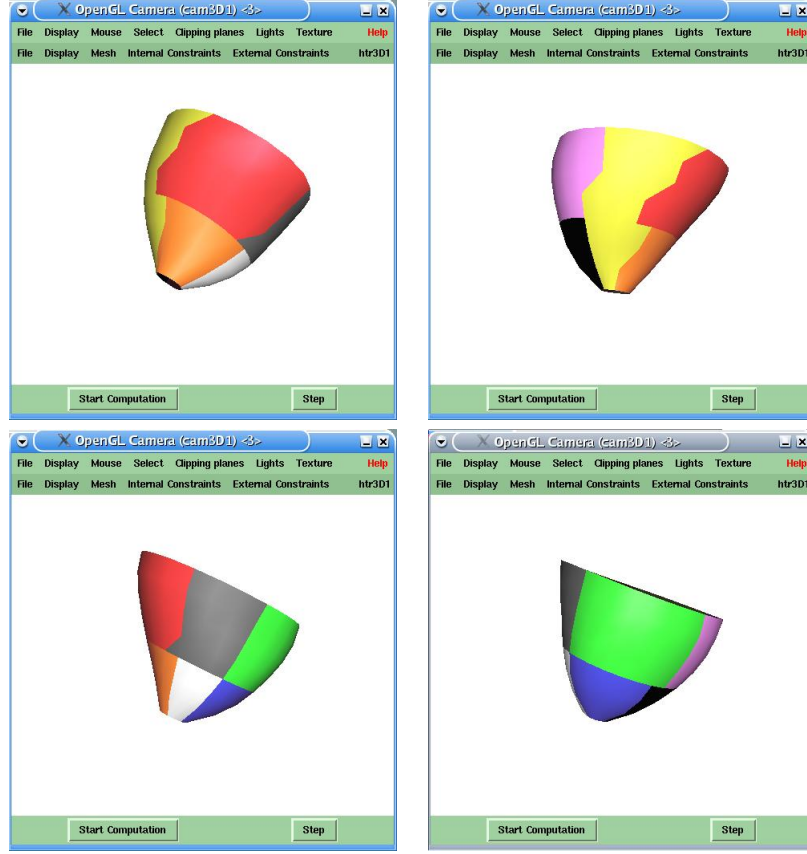


Figure 23: The 9 regions chosen on the epicardium, according to the propagation of the depolarization wave. Different views. The red region includes the pacing electrodes.

We create a partition of the epicardium into 9 regions according to the electrical propagation. In practice, we split the epicardium in successive regions following the isolines of the depolarization times map as closely as allowed by the mesh resolution. But these regions are very large. Moreover, there is no reason why the electrical conductivity should be constant on these large regions. Therefore we split these regions orthogonally to the isolines like in Figure 23.

We then estimate one conductivity value for each region successively. We apply algorithm 2 where $E(R)$ includes not only the vertices of R but also all its neighbors i.e. all the vertices that are linked by an edge to a vertex of R . We sort the 9 regions of Figure 23 in order to be sure that all the regions before the region we process have already been estimated. The convergence on each region is presented in Figure 24.

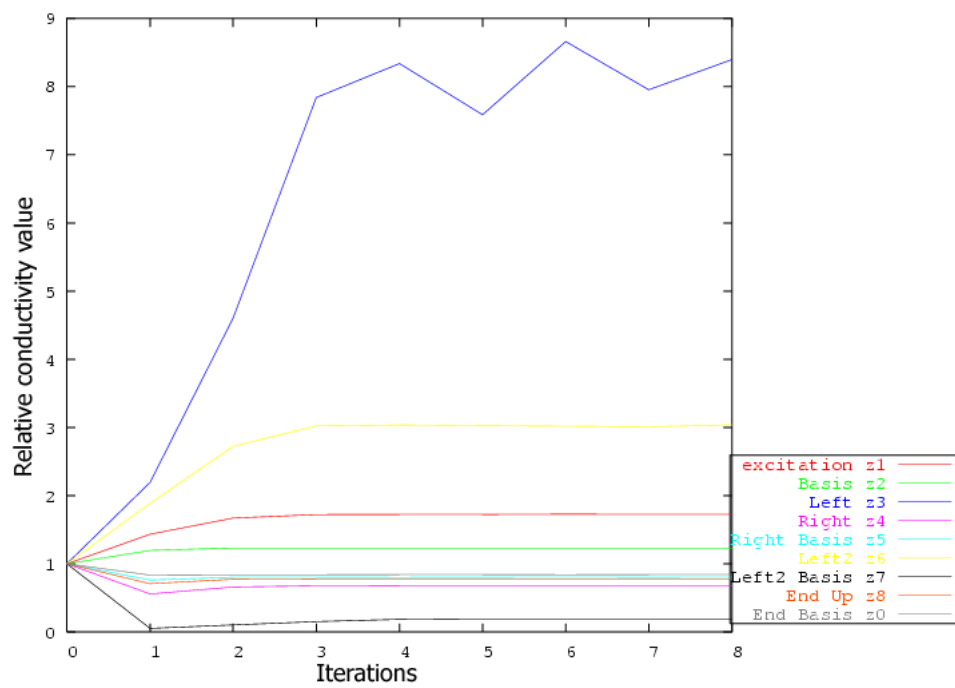


Figure 24: Convergence of the conductivity for the 9 selected regions

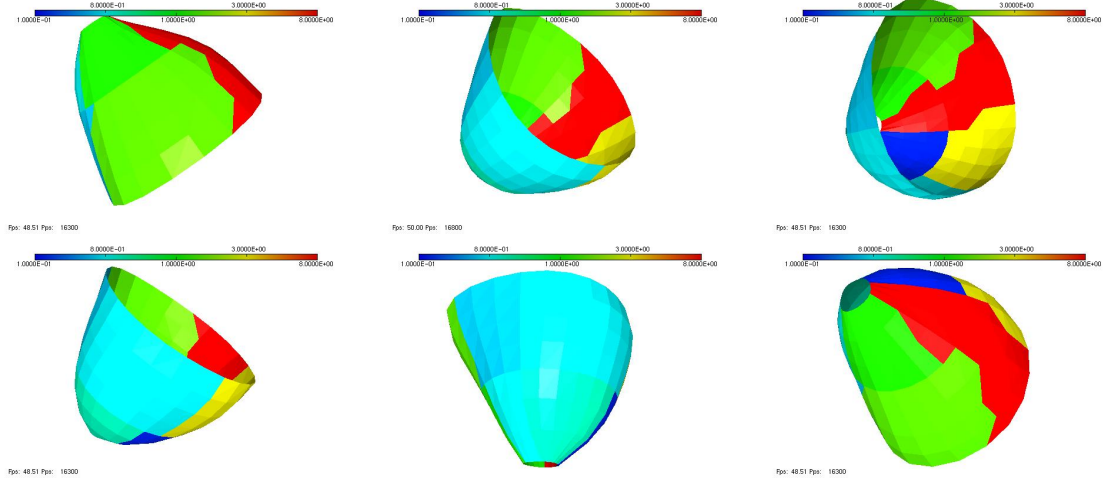


Figure 25: Conductivity map. Different views. The color represents the conductivity value. From blue (small values) to red (high values).

5.7 Relevance of the computed conductivity

Figure 25 presents the conductivity map that we obtained with different views. As we can see with Figures 24 and 25, a conductivity value around 1.0 has been assigned to most regions (between 0.8 and 1.8). We expected such a result since the measures are from a normal canine heart.

We focus on the first region, which includes the pacing electrodes. In this region, we had a problem with the global estimation because the depolarization appears to be faster than in the other of the epicardium whereas the model with constant parameters is not able to capture this phenomenon. Fortunately with the local estimation, the conductivity value estimated in this region is higher than 1.0, producing a faster depolarization wave in the pacing region, in perfect agreement with the experiment.

Moreover, we are able to detect that the measures present a dissymmetry: the depolarization wave is faster on one side than on the other side. This is visible both from the depolarization times and from velocity computation. This may be due to the fact that we model the epicardium as an homogeneous medium, without distinguishing the left and right ventricle nor taking into account the fiber directions. Nevertheless, our estimation provides us with dissymmetric conductivities. On the upper right view of Figure 25, the green region corresponds to the pacing region. On the left, we estimate a conductivity close to 0.9, whereas on the right we estimate a conductivity close to 8.0. If we refer to Equation 4, it means that the propagation velocity is approximately three times greater on one side than on the other ($\sqrt{8/0.9} \approx 2.98$).

	mean absolute error on depolarization times
Without any quantitative adjustment	0.0206 s
With only a global adjustment	0.0109 s
With global and local adjustment	0.0049 s

Table 1: Mean absolute error on depolarization times, computed on the entire epicardium.

Finally, we also estimate a very low conductivity on one region (the blue one in Figure 25). But this region comes just after the high conductivity region (the red one in Figure 25). It means that the red region was certainly too large, and the value we estimated was not accurate for the entire region. So the low value was obtained because the algorithm was trying to compensate for the advance taken when the depolarization wave was crossing the red region.

5.8 Accuracy of the depolarization times

Table 1 summarizes the absolute error on depolarization times before and after each step of the process. We can see that the absolute error decreased significantly both after the global estimation and the local estimation. For a comparison, we can recall that the duration of the depolarization wave is about 0.12 s. But the mean error is not the best criterion to judge the impact of the local estimation. Figure 26 displays the histograms of the absolute error before and after the local estimation of the conductivity. We notice that the maximum error has significantly decreased with the local estimation. Moreover, we observe a smaller dispersion of the error with the local adjustment. Figures 27 and 28 displays the depolarization times simulated by the model before (Figures 27(a) and 28(a)) and after (Figures 27(b) and 28(b)) the local estimation of the conductivity compared with the measures (Figure 27(c) and 28(c)). Figure 29 displays the absolute error on the depolarization times before and after the local estimation of the conductivity.

From Figures 27 and 28, we notice a visual improvement of the depolarization times. Comparing these results with the measures (Figures 27(c) and 28(c)), we notice that the shape of the depolarization times map is much closer to the measures with the local adjustment. The quality of this estimation is also assessed by the visualization of the absolute error on the depolarization times in the epicardial surface. On Figure 29(a), the error on the depolarization times is small near the pacing region but becomes larger further away from this region. The final error on the depolarization times (Figure 29(b)) is not only smaller but also more homogeneous. Thus the agreement between the measures and the model is improved in the entire epicardial surface. In conclusion, the error has been considerably improved by the local estimation of the conductivity, even if we only added 9 degrees of freedom: 9 conductivity values for 9 regions.

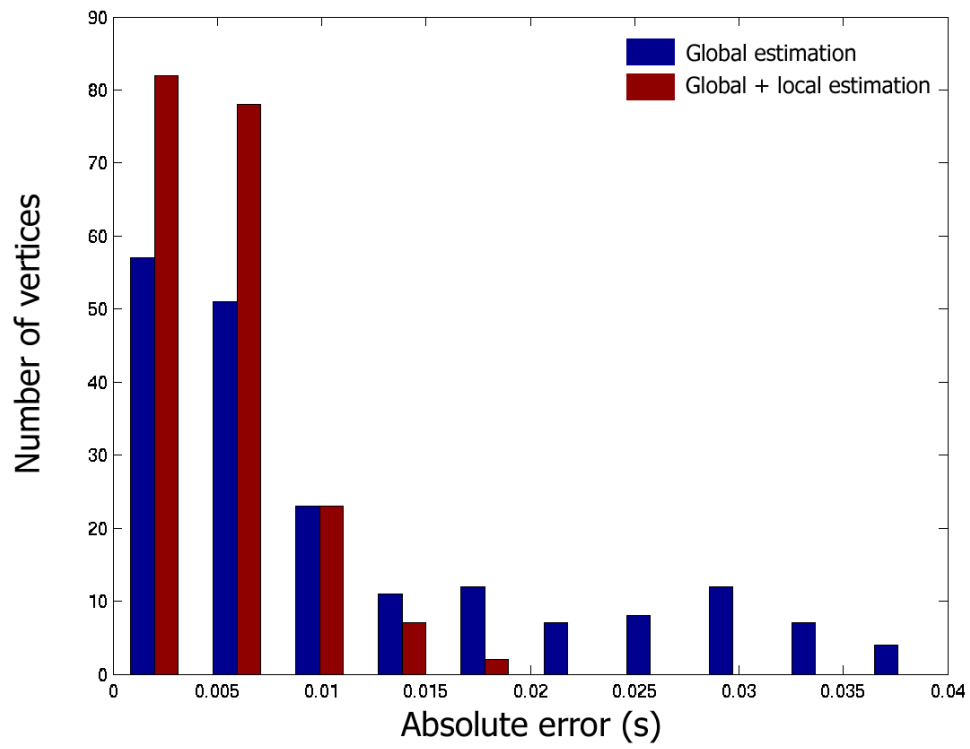


Figure 26: Histograms of the absolute error on the depolarization times. The error resulting from a global estimation is represented by the blue rectangles. The final error with both global and local adjustment is displayed in red.

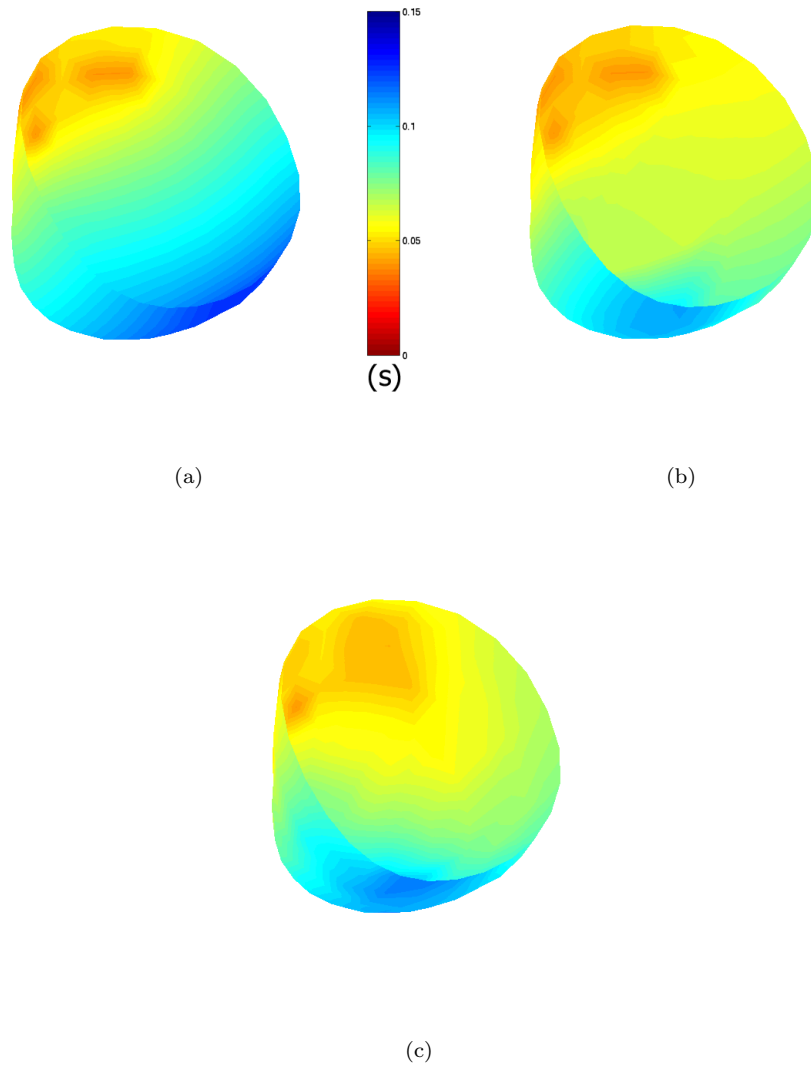


Figure 27: Depolarization times before (a) and after (b) the local estimation compared with the measures (c).

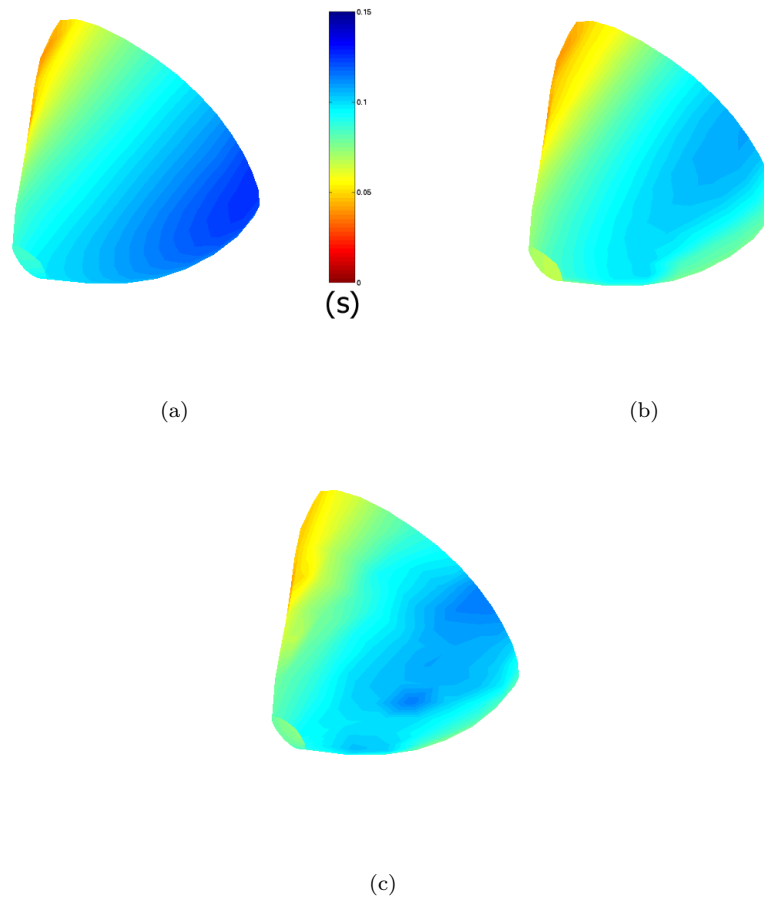
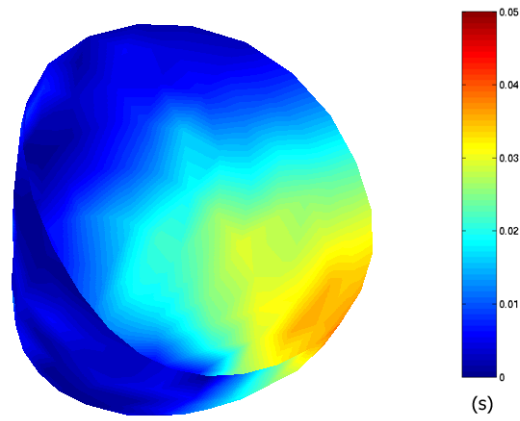
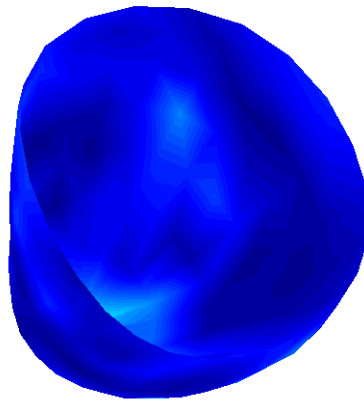


Figure 28: Depolarization times from a second point of view : before (a) and after (b) the local estimation compared with the measures (c).



(a)



(b)

Figure 29: Absolute error on the depolarization times before (a) and after (b) the local estimation of the parameters.

6 Conclusions and perspectives

We addressed the problem of estimating a set of parameters for the action potential propagation modeled by Aliev and Panfilov from measured depolarization times. In order to evaluate the quality of our results, we used a criterion based on the difference of the depolarization times between the model and the electrical measures. We first presented a procedure to estimate globally a set of parameters so that the electrical propagation in the model occurs in the same time and space scale as the measures. We used the theoretical properties of the Aliev and Panfilov system and validated the approach on simulated depolarization times. We then presented a method described in Algorithm 2 to estimate locally the electrical conductivity region by region. This method was validated on simple simulated depolarization times. We then presented electric measures performed *in vivo* on a canine heart. We successfully applied the global and local parameter estimation for these measures. The simulation of the model with these new values showed that the error on the depolarization times between the measures and the model were significantly decreased. Moreover, the conductivity values that we obtained seemed plausible even if a ground truth is not available.

In order to have a totally automatic process, we still have to build automatically the partition of the epicardium. We also need to take into account the anisotropy caused by myocardium fibers. The next step will be to estimate the parameters of a 3D model of the heart by establishing a correspondence between 2D measures and a 3D mesh. A really physiological validation would require to apply our method to a benchmark of pathologic and normal measures analysed by experts. This method seems to take good advantage of the depolarization times. For the moment, only the conductivity is estimated. But other measures like the action potential duration would allow us to estimate more parameters. A great advantage of the local estimation of the conductivity that we proposed is that it uses the model nearly as a black box. Thus, we will be able to apply it to more complex models, in order to deal with other electrical pathologies.

Acknowledgments

This work was partially funded by the scientific direction of INRIA through the Cooperative Research Action ICEMA2 (<http://www-rocq.inria.fr/sosso/icema2/icema2.html>). This action involved several partners including the INRIA research groups CAIMAN, EPIDAURE, MACS and SOSSO and was coordinated by Fr  d  rique Cl  ment(SOSSO).

Appendix A: Numerical implementation of the finite elements methods

The spatial integration is done with the finite elements method. We use linear triangular elements with 3 vertices. For the action potential u , that means that for each point \mathbf{P} in

the surface:

$$u(\mathbf{P}) = \sum_{i=0}^{N-1} \varphi_i(\mathbf{P}) u_i \quad (20)$$

where u_i is the value at the vertex i and φ_i is the basis function associated to the vertex i . The functions φ_i are linear. On each triangle, the value u is a linear interpolation of the values at the vertices. For \mathbf{P} in the triangle $(\mathbf{P}_0 \mathbf{P}_1 \mathbf{P}_2)$,

$$u(\mathbf{P}) = \sum_{i=0}^2 \varphi_i(\mathbf{P}) u(\mathbf{P}_i). \quad (21)$$

$(\varphi_i(P))_{0 \leq i \leq 2}$ are the barycentric coordinates of the point \mathbf{P} in the triangle $(\mathbf{P}_0 \mathbf{P}_1 \mathbf{P}_2)$. $\varphi_i(\mathbf{P})$ also is the area of the triangle $(\mathbf{P} \mathbf{P}_1 \mathbf{P}_2)$ (cf Figure 30):

$$\varphi_i(\mathbf{P}) = -\frac{\mathbf{S}_i}{2\mathcal{A}} \cdot (\mathbf{P} - \mathbf{P}_{i+1}) \quad (22)$$

where \mathcal{A} is the area of the triangle $(\mathbf{P}_0 \mathbf{P}_1 \mathbf{P}_2)$ and $\mathbf{S}_i = l_i \mathbf{n}_i$. Where l_i is the length of the segment $\mathbf{P}_{i+1} \mathbf{P}_{i+2}$ and \mathbf{n}_i is the external normal to this segment (cf. Figure 30). The basis functions are linear. Their gradient is therefore constant on each triangle as we can see with Equation (22). This gradient is given by

$$\nabla \varphi_i(\mathbf{P}) = -\frac{\mathbf{S}_i}{2\mathcal{A}}$$

As a consequence we can compute the gradient of any quantity in the surface mesh. Let θ be a function defined on the mesh, then the spatial gradient $\nabla \theta(\mathbf{P})$ for each point \mathbf{P} in the triangle $(\mathbf{P}_0 \mathbf{P}_1 \mathbf{P}_2)$ is given by

$$\nabla \theta(\mathbf{P}) = \sum_{i=0}^2 \theta(\mathbf{P}_i) \nabla \varphi_i \quad (23)$$

The mass matrix \mathcal{M} , and the rigidity matrix \mathcal{K} are:

$$\begin{cases} \mathcal{M}_{ij} &= \int_{\Omega} \varphi_i \varphi_j \\ \mathcal{K}_{ij} &= \int_{\Omega} d \nabla \varphi_i \nabla \varphi_j \end{cases} \quad (24)$$

where d is the conductivity. One conductivity value is assigned to each triangle. Therefore, the electrical conductivity d is a piecewise constant function, it is constant on each triangle. The matrix \mathcal{M} is further approximated to be a diagonal matrix (mass lumping). Consequently, the mass of each vertex is a third of the sum of the area of the triangles where they belong. The rigidity matrix \mathcal{K} can be computed easily. Let $\mathcal{SH}(i, j)$ be the shell of the edge (i, j) , that is the set of the triangles to which the edge belongs.

$$\mathcal{K}_{ij} = \sum_{tr \in \mathcal{SH}(i, j)} d(tr) \nabla \varphi_i(tr) \nabla \varphi_j(tr).$$

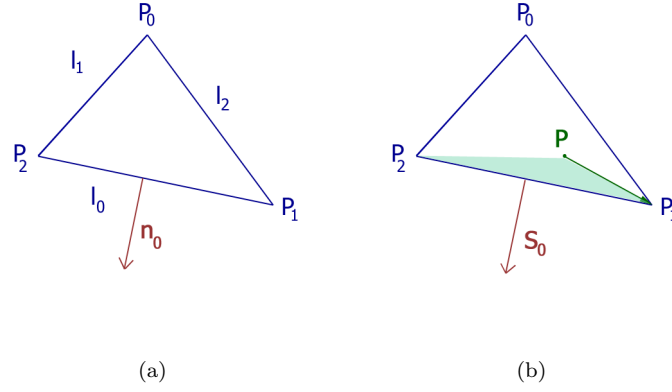


Figure 30: Notations used on a triangle $(\mathbf{P}_0\mathbf{P}_1\mathbf{P}_2)$. $\varphi_0(\mathbf{P}) = \mathcal{A}(PP_1P_2)$.

The temporal integration of the system (1) is done with an explicit Euler scheme.

$$\begin{cases} u^{t+\Delta t} &= u^t + \frac{\Delta t}{\varepsilon} [-l^2 \varepsilon^2 \mathcal{M}^{-1} \mathcal{K} u^t (1 - u^t)(u^t - a) - u^t z^t] \\ z^{t+\Delta t} &= z^t + \Delta t [-k u^t (u^t - a - 1) + z^t] \end{cases} \quad (25)$$

Then for each vertex i ,

$$\begin{cases} u_i^{t+\Delta t} &= u_i^t + \frac{\Delta t}{\varepsilon} [-l^2 \varepsilon^2 \mathcal{M}_{ii}^{-1} \sum_{j \in J} \mathcal{K}_{ij} u_j^t (1 - u_i^t)(u_i^t - a) - u_i^t z_i^t] \\ z_i^{t+\Delta t} &= z_i^t + \Delta t [-k u_i^t (u_i^t - a - 1) + z_i^t] \end{cases} \quad (26)$$

where J is the set of the indexes of the neighbors of the vertex i including the vertex i .

References

- [ACC⁺01] N. Ayache, D. Chapelle, F. Clément, Y. Coudière, H. Delingette, J.A. Désidéri, M. Sermesant, M. Sorine, and J. Urquiza. Towards model-based estimation of the cardiac electro-mechanical activity from ECG signals and ultrasound images. In T. Katila, I. Magnin, P. Clarysse, J. Montagnat, and J. Nenonen, editors, *Functional Imaging and Modelling of the Heart (FIMH'01)*, number 2230 in Lecture Notes in Computer Science (LNCS), pages 120–127. Springer, 2001. [2.1](#)
- [AP96] R.R. Aliev and A.V. Panfilov. A simple two-variables model of cardiac excitation. *Chaos, Soliton and Fractals*, 7(3):293–301, 1996. [1](#), [1.1](#), [2.1](#), [2.1](#), [3.2](#)

- [BABC96] A. L. Bardou, P. M. Auger, P. J. Birkui, and J.-L. Chassé. Modeling of cardiac electrophysiological mechanisms: from action potential genesis to its propagation in myocardium. *Critical Reviews in Biomedical Engineering*, 24:141–221, 1996. [2.1](#)
- [BBH⁺03] K. Brusdal, J.M. Brankart, G. Halberstadt, G. Evensen, P. Brasseur, P.J. van Leeuwen, E. Dombrowski, and J. Verron. A demonstration of ensemble based assimilation methods with a layered OGCM from the perspective of operational ocean forecasting systems. *Journal of Marine Systems*, 40-41:253–289, 2003. [2](#)
- [BEW03] L. Bertino, G. Evensen, and H. Wackernagel. Sequential data assimilation techniques in oceanography. *International Statistical review*, 71:223–241, 2003. [2](#)
- [BM04] M.E. Belik and A.D. McCulloch. *Handbook of Numerical Analysis, Computational of the Human Body*, chapter Computational methods for cardiac electrophysiology. 2004. [1](#), [2.1](#)
- [BR77] G.W. Beeler and H. Reuter. Reconstruction of the action potential of ventricular myocardial fibres. *Journal of Physiology*, 268(1):177–210, 1977. [2.1](#)
- [BWZ⁺02] O. Bernus, R. Wilders, C.W. Zemlin, H. Verschelde, and A.V. Panfilov. A computationnally efficient electrophysiological model of human ventricle cells. *Am J Physiol HeartCirc Physiol*, 282(6):2296–2308, 2002. [1](#), [2.1](#)
- [CCG⁺01] D. Chapelle, F. Clément, F. Génot, P. Le Tallec, M. Sorine, and J. Urquiza. A physiologically-based model for the active cardiac muscle contraction. In T. Katila, I. Magnin, P. Clarysse, J. Montagnat, and J. Nenonen, editors, *Functional Imaging and Modelling of the Heart (FIMH'01)*, number 2230 in Lecture Notes in Computer Science (LNCS), pages 128–133. Springer, 2001. [2.1](#)
- [CFGPT98] P. Colli Franzone, L. Guerri, M. Pennacchio, and B. Taccardi. Spread of excitation in 3-D models of the anisotropic cardiac tissue. III. Effects of ventricular geometry and fiber structure on the potential distribution. *Mathematical Biosciences*, 151(1):51–98, 1998. [1](#)
- [Fit61] R.A. FitzHugh. Impulses and physiological states in theoretical models of nerve membrane. *Biophysical Journal*, 1:445–466, 1961. [2.1](#)
- [FK98] F. Fenton and A. Karma. Vortex dynamics in three-dimensional continuous myocardium with fiber rotation-filament instability and fibrillation. *Chaos*, 8:20–47, 1998. [2.1](#)
- [Kal60] R.E. Kalman. A new approach to linear filtering and prediction problems. *ASME Trans.-Journal of Basic Engineering*, 82:35–45, 1960. [2](#)

- [Kee86] J.P. Keener. A geometrical theory for spiral waves in excitable media. *SIAM Journal in Applied Mathematics*, 46(6):1039–1056, 1986. 2.3, 3.1
- [KFB⁺03] R.C.P Kerckhoffs, O. Faris, P.H.M. Bovendeerd, F.W. Prinzen, K. Smits, E.R. McVeigh, and T. Arts. Timing of depolarization and contraction in the canine paced ventricle: model and experiment. *Journal of Cardiovascular Electrophysiology*, 14:188–195, 2003. 1, 1.1
- [KPE04] V. Krinski, A. Pumir, and I. Efimov. *Encyclopedia of nonlinear science*, chapter Cardiac muscle models. Routledge, September 2004. 1, 2.1
- [Lio68] J.L. Lions. *Contr  le optimal de syst  mes gouvern  s par des   quations aux d  riv  es partielles*. Dunod, 1968. 1
- [LR91] C.H. Luo and Y. Rudy. A model of the ventricular cardiac action potential. Depolarization, repolarization and their interaction. *Circulation Research*, 68(6):1501–1526, 1991. 2.1
- [LR94] C.H. Luo and Y. Rudy. A dynamic model of the cardiac ventricular action potential - simulations of ionic currents and concentration changes. *Circulation Research*, 74(6):1071–1097, 1994. 2.1
- [May79] P.S. Maybeck. *Stochastic models, estimation and control*. Academic Press, 1979. 2
- [MFE⁺01] E. McVeigh, O. Faris, D. Ennis, P. Helm, and F. Evans. Measurement of ventricular wall motion, epicardial electrical mapping, and myocardial fiber angles in the same heart. In T. Katila, I. Magnin, P. Clarysse, J. Montagnat, and J. Nenonen, editors, *Functional Imaging and Modeling of the Heart (FIMH’01)*, number 2230 in Lecture Notes in Computer Science (LNCS), pages 76–82. Springer, 2001. 1, 1.1
- [MSTM01] A. McCulloch, D. Sung, M.E. Thomas, and A. Michailova. Experimental and computational modeling of cardiac electromechanical coupling. In T. Katila, I.E. Magnin, P. Clarysse, J. Montagnat, and J. Nenonen, editors, *Functional Imaging and Modeling of the Heart (FIMH’01)*, number 2230 in Lecture Notes in Computer Science, pages 113–119. Springer, 2001. 1, 1.1
- [Mur02] J.D. Murray. *Mathematical biology, 1: an introduction*. Springer, 2002. 2.3
- [Nob02] D. Noble. Modeling the heart from genes to cells to the whole organ. *Science*, 295:1678–1682, march 2002. 1, 2.1
- [NR01] D. Noble and Y. Rudy. Models of cardiac ventricular action potentials: iterative interaction between experiment and simulation. *Phil. Trans. R. Soc. Lond. A*, pages 1127–1142, 2001. 2.1

- [OEE⁺03] O.Faris, F. Evans, D. Ennis, P. Helm, J. Taylor, A. Chesnik, M.A. Guttman, C. Ozturk, and E. McVeigh. A novel technique for cardiac electromechanical mapping with MRI tagging and an epicardial electrode sock. *Annals of Biomedical Engineering*, 31(4):430–440, 2003. [5.1](#)
- [PVR97] D.T. Pham, J. Verron, and M.C. Roubaud. Singular evolutive Kalman filter with EOF initialization for data assimilation in oceanography. *Journal of Maritime Systems*, 1997. [2](#)
- [RP82] T.C. Ruch and H.D. Patton, editors. *Physiology and Biophysics*. W. B. Saunders, 20th edition, 1982. [2.1](#), [2](#)
- [Rud01] Y. Rudy. *Heart Physiology and Pathophysiology*, chapter Electrocardiogram and Cardiac Excitation, pages 133–148. Academic Press, 2001. [1.2](#)
- [SCD⁺01] M. Sermesant, Y. Coudie're, H. Delingette, N. Ayache, and J.A. De'side'ri. An electro-mechanical model of the heart for cardiac image analysis. In W.J. Niessen and M.A. Viergever, editors, *4th Int. Conf. on Medical Image Computing and Computer-Assisted Intervention (MICCAI'01)*, volume 2208 of *LNCS*, pages 224–231, Utrecht, The Netherlands, October 2001. [2.1](#)
- [SFE⁺03] M. Sermesant, O. Faris, F. Evans, E. McVeigh, Y. Coudière, H. Delingette, and N. Ayache. Preliminary validation using in vivo measures of a macroscopic electrical model of the heart. In N. Ayache and H. Delingette, editors, *International Symposium on Surgery Simulation and Soft Tissue Modeling (IS4TM'03)*, volume 2673, pages 230–243, Juan-les-Pins, France, 2003. INRIA Sophia Antipolis, Springer-Verlag. [1.1](#), [2.1](#)
- [SFP⁺02] Maxime Sermesant, Clément Forest, Xavier Pennec, Hervé Delingette, and Nicholas Ayache. Biomechanical model construction from different modalities: Application to cardiac images. In Takeyoshi Dohi and Ron Kikinis, editors, *Medical Image Computing and Computer-Assisted Intervention (MICCAI'02)*, volume 2488 of *LNCS*, pages 714–721, Tokyo, September 2002. Springer. [2.1](#)
- [SL02] Pengcheng Shi and Huafeng Liu. Stochastic finite element framework for cardiac kinematics function and material property analysis. In Takeyoshi Dohi and Ron Kikinis, editors, *MICCAI'02*, volume 2488 of *Lecture Notes in Computer Science*, pages 635–641, Tokyo, September 2002. Springer. [4.1](#)
- [SNH01] K. Simelius, J. Nenonen, and B.M. Horáček. Simulation of anisotropic propagation in the myocardium with a hybrid bidomain model. In T. Katila, I. Magnin, P. Clarysse, J. Montagnat, and J. Nenonen, editors, *Functional Imaging and Modeling of the Heart (FIMH'01)*, number 2230 in *Lecture Notes in Computer Science (LNCS)*, pages 140–147. Springer, 2001. [1](#), [1.1](#), [2.1](#)

-
- [TNNP03] K. H.W.J. Ten Tusscher, D. Noble, P. J. Noble, and A. V. Panfilov. A model for human ventricular tissue. *Am J Physiol Heart Circ Physiol*, 286(4):1573–1589, December 2003. [1](#)
- [Tun78] L. Tung. *A bidomain model for describing ischemic myocardial D-C potentials*. PhD thesis, MIT Cambridge, Massachusetts, 1978. [2.1](#)
- [vdMW01] R. van der Merwe and E.A. Wan. The square root unscented Kalman filter for state and parameters estimation. In *International Conference on Acoustics, Speech and Signal Processing (ICASSP)*, May 2001. [2](#)



Unité de recherche INRIA Sophia Antipolis
2004, route des Lucioles - BP 93 - 06902 Sophia Antipolis Cedex (France)

Unité de recherche INRIA Futurs : Parc Club Orsay Université - ZAC des Vignes
4, rue Jacques Monod - 91893 ORSAY Cedex (France)

Unité de recherche INRIA Lorraine : LORIA, Technopôle de Nancy-Brabois - Campus scientifique
615, rue du Jardin Botanique - BP 101 - 54602 Villers-lès-Nancy Cedex (France)

Unité de recherche INRIA Rennes : IRISA, Campus universitaire de Beaulieu - 35042 Rennes Cedex (France)

Unité de recherche INRIA Rhône-Alpes : 655, avenue de l'Europe - 38334 Montbonnot Saint-Ismier (France)

Unité de recherche INRIA Rocquencourt : Domaine de Voluceau - Rocquencourt - BP 105 - 78153 Le Chesnay Cedex (France)

Éditeur
INRIA - Domaine de Voluceau - Rocquencourt, BP 105 - 78153 Le Chesnay Cedex (France)
<http://www.inria.fr>
ISSN 0249-6399